Particuology 115 (2026) 126–147

Contents lists available at ScienceDirect

Particuology

journal homepage: www.elsevier.com/locate/partic

# A DEM-based study of particle-shape effects on compressibility and contact-scale response in idealized granular assemblies

Betül Poyraz, Ahmet Talha Gezgin *

*Department of Civil Engineering, Bursa Uludag University, Nilüfer, Bursa, Turkey*

## HIGHLIGHTS

- A DEM-based comparative framework is used to examine shape-dependent compressibility in idealized granular assemblies.
- Stress-normalized macro- and micro-scale indicators clarify particle-shape effects under different vertical stress levels.
- The normalized macro-scale stiffness response shows a non-monotonic trend with particle shape factor.
- Contact-scale statistics quantify force partitioning, coordination distribution, and local overlap characteristics.
- Shape-dependent compressibility is governed by combined contact-network, force-transfer, and deformation mechanisms.

## GRAPHICAL ABSTRACT

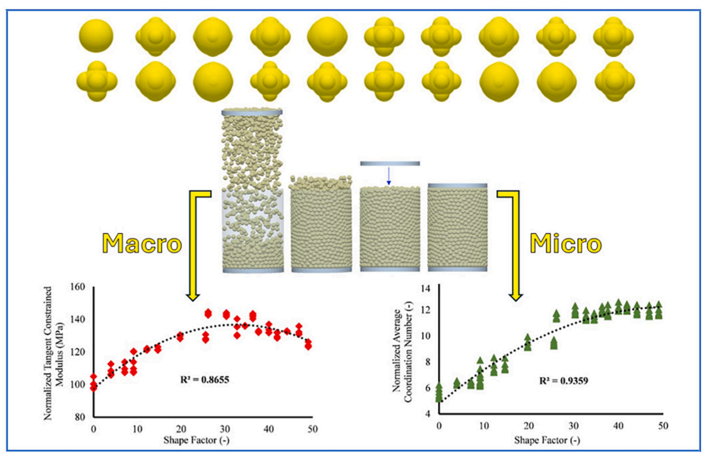


## ARTICLE INFO

*Keywords:*
Discrete element modeling
Particle shape
Compressibility
Coordination number
Stress normalization
Contact force

## ABSTRACT

This study employs a benchmarked Discrete Element Method model to investigate the influence of particle shape on the compressibility behavior of granular assemblies within a controlled comparative framework. Twenty idealized particle geometries with different shape characteristics were analyzed under constrained compression at vertical stress levels ranging from 0.1 to 3.2 MPa. Macro- and micro-scale responses were evaluated using constrained modulus and average coordination number, together with additional contact-scale analyses to improve the interpretation of particle-scale behavior. The results indicate that both macro- and micro-scale responses remain strongly stress-dependent, suggesting that conventional indicators alone cannot fully isolate particle-shape effects. A stress-normalized scaling approach was therefore applied to reduce the dominant influence of stress and clarify geometry-related trends. The analyses demonstrate that increasing particle irregularity promotes denser contact networks, redistributes contact forces across more contacts, and alters local deformation mechanisms. The findings provide a comparative DEM-based assessment of shape-dependent compressibility and contact-scale force–deformation behavior in idealized granular assemblies.

* Corresponding author.
*E-mail address:* ahmettalhagezgin@uludag.edu.tr (A.T. Gezgin).

https://doi.org/10.1016/j.partic.2026.05.010
Received 26 February 2026; Received in revised form 3 May 2026; Accepted 12 May 2026
Available online 22 May 2026

## 1. Introduction

Granular materials are of critical importance in various applications, including construction, mining, agriculture, food, and pharmaceutical industries, due to their heterogeneous structures formed by the interaction of numerous discrete particles (Hill & Selvadurai, 2005). Despite being in the solid phase, they exhibit unique mechanical characteristics that differ from classical solid–liquid behavior due to the interparticle voids and contact forces (Jaeger et al., 1996; O'Sullivan, 2011). The macroscopic behavior of granular materials results from the combination of interparticle interactions and is directly related to their microstructural properties (Santamarina, 2003). This interdependence between particle-scale interactions and macro-scale response has also been emphasized in several micromechanical studies, which have demonstrated that fabric, contact arrangement, and force-transmission pathways critically shape the macroscopic stress–strain behavior (Durán et al., 2010; Li & Yu, 2013; Zhao & Li, 2025). This microstructure is formed by the combined effects of various factors, including particle shape, size distribution, contact geometry, packing density, force-transmission pathways, and the applied stress level (Radjai et al., 2012). These contact properties shape force chains and contact networks at the meso-scale and, in turn, determine the compressibility, strength, and deformation properties of the material at the macro-scale (Basak et al., 2021; Lee et al., 2025; Zhao, Zhao, & Luding, 2023). In particular, the anisotropic distribution of strong-force chains observed in 3D granular systems has been shown to play an important role in stiffness and deformation resistance (Antony & Kuhn, 2004). The coordination number is one of the fundamental indicators that quantitatively define this contact organization, serving as a measure of the average number of interparticle contacts (Gezgin, 2025; Gezgin et al., 2022). An increasing coordination number represents the continuity of load transfer paths and the homogeneity of stress distribution, and is therefore considered an important micromechanical indicator of the material's deformation resistance (Basak et al., 2021; Lee et al., 2025). Therefore, in order to reliably model the behavior of granular materials, the relationship between the micro and macro scales must be investigated using a consistent framework linking contact organization to assembly-level response (Hatefi et al., 2024; Liu et al., 2025).

Particle shape is one of the most effective geometric parameters that determines critical engineering behaviors of granular materials, such as strength, compressibility, permeability, expansion, and liquefaction (Alshibli & Cil, 2018; Altuhafi et al., 2016; Banala et al., 2019; Danesh et al., 2020; Peng et al., 2021; Zhao, Zhao, & Luding, 2023). Recent DEM studies have further demonstrated that deviations from spherical geometry significantly influence shear strength, fabric anisotropy, and particle rotation patterns (Ng et al., 2018; Nie et al., 2020). Shape parameters directly affect both micro-scale force transmission pathways and macro-scale deformation responses by altering the contact configuration. Compressibility is one of the most prominent properties that exhibits these effects, serving as a fundamental indicator of stiffness and resistance to volume change under load (Mesri & Vardhanabhuti, 2009; Zeng et al., 2025). The elastic modulus (or volumetric elasticity modulus) at the macro scale and the contact stiffness, coordination number, and distribution of contact forces at the micro scale are used to define compressibility (Hatefi et al., 2024; Ulusoy, 2023). However, findings in the literature regarding the effect of particle shape on compressibility are inconsistent. While some studies suggest that more angular particles fracture more easily at lower stress levels and exhibit higher compressibility (Karimpour-Fard et al., 2021; Sharma et al., 2021), others report that increased shape irregularity strengthens internal locking and increases volumetric deformation resistance (Koutous & Hilali, 2019; Sarkar et al., 2019). Such conflicts are compatible with recent findings indicating that morphological effects cannot be evaluated independently of stress history, as stress-induced pattern evolution and contact reorganization may mask or enhance mechanisms related to shape characteristics (Cheng et al., 2020). These conflicting results suggest that the effect of particle shape should be evaluated not only in terms of geometric irregularity but also in conjunction with the applied stress level.

The Discrete Element Method (DEM) stands out as a powerful tool for analyzing the microstructural properties and macroscopic behavior of granular materials, owing to its ability to resolve detailed particle motion and contact interactions (Cundall & Strack, 1979). This enables the quantitative determination of parameters that are difficult to measure experimentally, such as coordination number, contact stiffness, and local stress distribution, and allows for the direct linking of macro-scale deformation responses to micro-level interactions (Gezgin et al., 2021, 2022). Studies in the literature demonstrate that DEM models, when appropriately benchmarked or validated for the problem of interest, facilitate a detailed examination of the relationships between particle morphology, contact organization, and stiffness (Hatefi et al., 2024; Zhao, Zhao, & Luding, 2023).

Current research has shown that particle shape significantly affects stiffness and coordination number; however, quantitative, comprehensive models describing how this relationship changes with stress levels are limited. While some studies report that shape irregularity increases coordination number and macro rigidity (He & Guo, 2018; Wiącek et al., 2012; Zhao et al., 2023), others indicate that excessive irregularity weakens the contact network under low stress conditions (Kodicherla et al., 2019). These findings suggest that the effect of shape on compressibility must be evaluated in conjunction with stress conditions. However, there is a lack of studies in the literature that model particle shape and stress effects simultaneously within a comparative quantitative framework. Moreover, many DEM-based interpretations of particle-shape effects rely mainly on average microstructural indicators or qualitative contact-network visualizations, whereas quantitative contact-scale descriptors such as weak–strong contact partitioning, mean contact-force scaling, coordination-number distributions, and local overlap statistics are less frequently integrated into a unified micro-to-macro interpretation. This limitation makes it difficult to distinguish shape-related trends from stress-dependent responses, as particle rearrangement dominates the response at low stress levels, whereas locking and contact-geometry effects emerge only beyond certain stress thresholds. Consequently, how to normalize such stress-dependent shape effects within a single mathematical framework remains insufficiently explored.

In this study, regression analysis is employed as a quantitative tool within a DEM-based comparative framework to express stress-normalized particle-shape effects on granular compressibility. This approach enables the statistical correlation of micro- and macro-scale indicators, such as tangent constrained modulus and coordination number, with particle shape and stress parameters, thereby rendering the role of particle geometry in compressibility more comparable within the controlled conditions of the numerical analyses (El-Kassem et al., 2021; Mata, 2011; Sharma & Singh, 2018). In addition to these stress-normalized macro- and micro-scale indicators, the present revision incorporates quantitative contact-scale statistics to better clarify the mechanisms underlying the observed compressibility trends. These statistics include coordination-number distributions, weak-contact percentages, average normal contact force–stress relationships, a stress-normalized mean contact-force coefficient, and normalized normal-overlap descriptors.

This study aims to quantitatively examine the stress-normalized influence of particle shape on the compressibility behavior of granular materials using a DEM-based approach. Accordingly, particle models with different SF and AF values were created. The macro-scale tangent-constrained modulus and micro-scale average coordination number were evaluated under a continuously applied confined compression path. In addition, contact-scale force, coordination, and deformation characteristics were quantified for selected representative particle shapes to strengthen the micro-scale interpretation beyond qualitative visualization. First, stress-induced trends were identified at both scales;

then, shape-related trends, after accounting for the dominant effect of stress, were quantified within a multivariate framework. To capture possible nonlinear effects of particle morphology, the regression model included both linear and quadratic terms (e.g., $SF^2$). The contact-scale analyses were further used to examine whether the observed macro-scale compressibility trends were associated with changes in coordination-number distributions, weak-contact fraction, mean force carried per contact, and local normal-overlap distribution. In this way, the role of particle shape in compressibility behavior at the micro- and macro-scales was evaluated through stress-normalized relationships, and a comparative quantitative framework was established to interpret shape-dependent compressibility trends in the analyzed granular assemblies. Accordingly, the present study should be interpreted as a controlled comparative DEM investigation of shape-dependent compressibility trends within an idealized particle family considered in this study, rather than as a universal predictive framework for natural granular materials.

## 2. Methodology

### 2.1. Overview of DEM framework

The Discrete Element Method (DEM) is a widely used numerical framework that models each particle in a granular assembly as an independent solid component, enabling the direct resolution of the micromechanical behavior of particulate systems. The method is based on the foundational principles proposed by Cundall and Strack (1979), which involve solving interparticle contact forces and the associated motions in accordance with Newton's second law of motion. Thus, without requiring assumptions about a continuous medium or a predefined stress-strain relationship, the macroscopic behavior of the assembly emerges directly from interparticle force transmission without invoking phenomenological constitutive laws.

The primary advantage of DEM is that it allows the detailed investigation of micromechanical processes that are often elusive to conventional experimental observations. Contact network formation, the development of force chains, local stress concentrations, and structural reorganizations can be tracked with high temporal and spatial resolution using this method (Ioannidi et al., 2024; Jiang et al., 2016; Xu et al., 2024). Furthermore, scale and boundary-condition effects encountered in laboratory experiments can be precisely controlled in numerical simulations, making the method a powerful tool for parametric analyses. However, numerical stability and computational efficiency require careful selection of time step, particle resolution, and contact parameters (Jing & Stephansson, 2007; Thakur et al., 2016).

The DEM algorithm operates through iterative time-step cycles. At each time step, contact detection is followed by force evaluation (normal and tangential components), and particle motion is updated via explicit time integration. To ensure numerical stability, the computational increment must be kept strictly below the critical threshold defined by the system's characteristic frequencies; otherwise, numerical instabilities may occur (Burns & Hanley, 2017).

The choice of contact model is a critical step that directly affects simulation accuracy. The contact model used to establish the force-displacement relationship between particles must be selected based on the specific physical properties of the granular media. Various contact formulations exist in the literature (Burns et al., 2019; Dimaio & Direnzo, 2005; Rojek, 2018), and the selected model governs both the macroscopic response and micromechanical indicators such as coordination number and contact-fabric evolution.

### 2.2. Development and benchmarking of DEM model for confined compression test

The DEM model used in this study was benchmarked against experimental data to assess its ability to reproduce the confined compression response of a reference spherical assembly. For this purpose, the confined compression experiment conducted by Chung (2006) with spherical glass beads served as the primary benchmarking case. In the experiment, glass beads were deposited into an acrylic container (145 mm diameter, 380 mm height). A displacement rate of 1.5 mm/min was applied to the top plate, and the forces transmitted to the boundaries were continuously monitored (Chung, 2006). This reference case was used to establish the DEM setup for the confined compression problem before extending the simulations to the idealized particle geometries considered in the present study.

All DEM simulations in this study were performed using the commercial software Altair Engineering Inc, (2022) Particle–particle and particle–wall interactions were modeled using the Hertz–Mindlin (no-slip) contact model, which provides a nonlinear contact formulation suitable for elastic granular assemblies. This model accounts for normal and tangential contact stiffness, damping coefficients, and Coulomb frictional slip, thereby resolving contact-scale force transmission. Material parameters were assigned according to the reference experimental study (Chung, 2006). Additionally, the computational cycle utilized the velocity-Verlet integration scheme. The time-step increment was maintained below 20% of the Rayleigh time step to ensure numerical stability.

The numerical model replicated the experimental configuration using a cylindrical container and rigid plates. A total of 3586 spherical particles were generated. A comparative summary of the material and contact parameters is provided in Table 1. As shown in the table, the Young's modulus was 41 GPa in the reference case. However, maintaining this value leads to an excessively small critical time step, increasing computational overhead to impractical levels. Therefore, the elastic modulus was scaled to 4.1 GPa to enhance computational efficiency. Because this scaling was applied uniformly to all contacts, the relative stress–strain trends were preserved while computational efficiency was substantially improved. Accordingly, the benchmarking exercise was intended to reproduce the overall compression response of the reference system rather than to replicate the original experiment at the contact level.

The benchmarking simulation followed a three-stage procedure. First, particles were deposited into the container using the air-pluviation method (Fig. 1a). To achieve this, the interparticle friction coefficient was set to zero during the deposition process to reach the target packing density. After filling, the second stage allowed the particles to settle freely until reaching a mechanically equilibrated state (Fig. 1b). At the end of the settling phase, the static friction coefficients were increased to 0.24. In the final stage, the top plate was displaced downward at a constant velocity of 2.5 mm/s without acceleration (Fig. 1c), and the compression process continued until the reaction force reached 800 N (Fig. 1d).

In the reference study, the loading rate was significantly lower;

**Table 1**
Input parameters of the reference study (Chung, 2006) and benchmarked model.

| Input parameters | Ref. study (Chung, 2006) | Benchmarked DEM model |
|---|---|---|
| Diameter of particles | 10 (mm) | 10 (mm) |
| Density of particles | 2530 ($kg/m^3$) | 2530 ($kg/m^3$) |
| Elastic modulus of particles | 41 GPa | 4.1 GPa |
| Poisson's ratio of particles | 0.22 | 0.22 |
| Static friction coefficient (glass bead – glass bead) | 0.24 | 0.24 |
| Static friction coefficient (glass bead – acrylic) | 0.24 | 0.24 |
| Restitution coefficient (glass bead – glass bead) | 0.79 | 0.79 |
| Restitution coefficient (glass bead – acrylic) | 0.79 | 0.79 |
| Number of glass beads | 3591 | 3586 |
| Velocity of the upper plate | 1.5 (mm/min) | 2.5 (mm/s) |

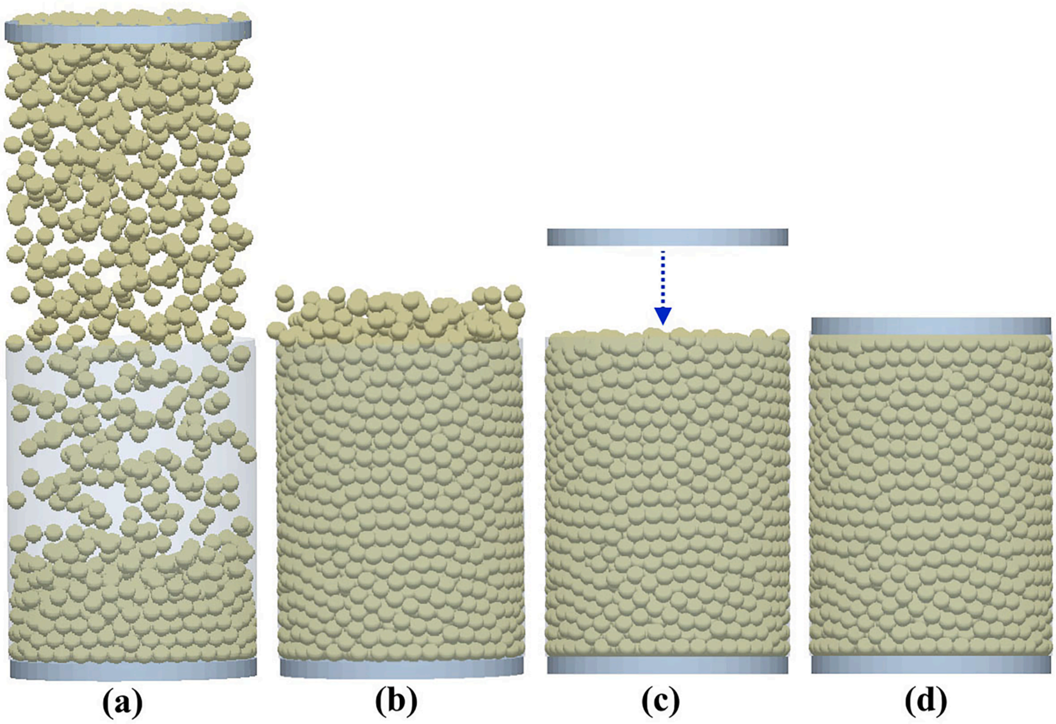


**Fig. 1.** Stages of specimen preparation in the DEM models.

however, a rate of 2.5 mm/s was adopted in the simulation to satisfy computational time constraints. To verify that the simulation remained under quasi-static conditions, the inertial effects were assessed by continuously monitoring the system's kinetic energy. Throughout the simulation, the kinetic energy remained several orders of magnitude lower than the work done by the boundary forces, confirming that the adopted loading rate preserves the quasi-static character of the compression process. The resulting force–displacement response was then compared with the experimental curves reported by Chung (2006), as presented in Fig. 2. In this figure, S1–S4 denote the four experimental force–displacement curves from the reference study, whereas DEM denotes the numerical response obtained from the present model. The resulting agreement provided a benchmarked DEM configuration for subsequent comparative analyses of the idealized particle family.

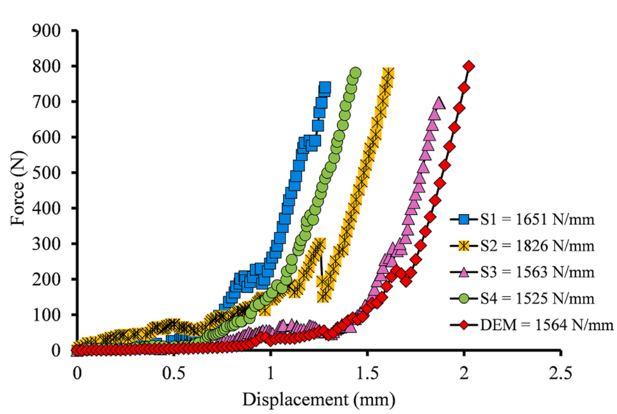


**Fig. 2.** Comparison between the force–displacement response of the DEM benchmarked model and the experimental force–displacement curves reported by Chung (2006). S1–S4 denote the four experimental curves from the reference study, and DEM denotes the numerical response obtained in the present study.

### *2.3. Generation and morphological characterization of particle geometries*

In this study, 20 particle models with varying geometric properties were created to investigate the effect of particle shape on compressibility. The approach proposed by Sukumaran and Ashmawy (2001) served as the basis for the quantitative definition of particle shapes. This method essentially involves discretizing the two-dimensional projection of the particle using equiangular sampling intervals and comparing it with a reference circle discretized using the same intervals. Thus, the particle shape can be described by two independent parameters: the shape factor (SF), which quantifies the deviation from a circle, and the angularity factor (AF), which accounts for sharp corners. This approach allows particle morphology to be defined in a scale-independent, reproducible, and comparable manner within a common projection-based sampling framework. Among the various shape descriptors available in the literature, this method was selected because it consistently quantifies both shape and angularity within a single sampling framework and has been widely adopted in DEM-based studies. In the present study, these descriptors were used to compare a controlled family of idealized particle geometries rather than to reproduce the full three-dimensional morphological complexity of natural granular particles.

To determine the SF and AF values of the generated particles, a systematic geometric discretization procedure was first implemented. As illustrated in Fig. 3(a), particle geometries were first generated in a controlled and parametric manner using one central circle and four symmetrically positioned neighboring circles with predefined dimensions in the x–y plane. The external boundary of the composite geometry was then extracted by retaining only the outer contour, as shown in Fig. 3(b), which represents the two-dimensional projection of the particle used for shape characterization. In the adopted method, the particle projection is discretized into radial segments extending from the center to the outer surface.

In this study, an equal angular sampling interval of 3° was employed, resulting in a total of 120 sampling directions (Fig. 3c). Although Sukumaran and Ashmawy (2001) judged N = 40 to represent a practical

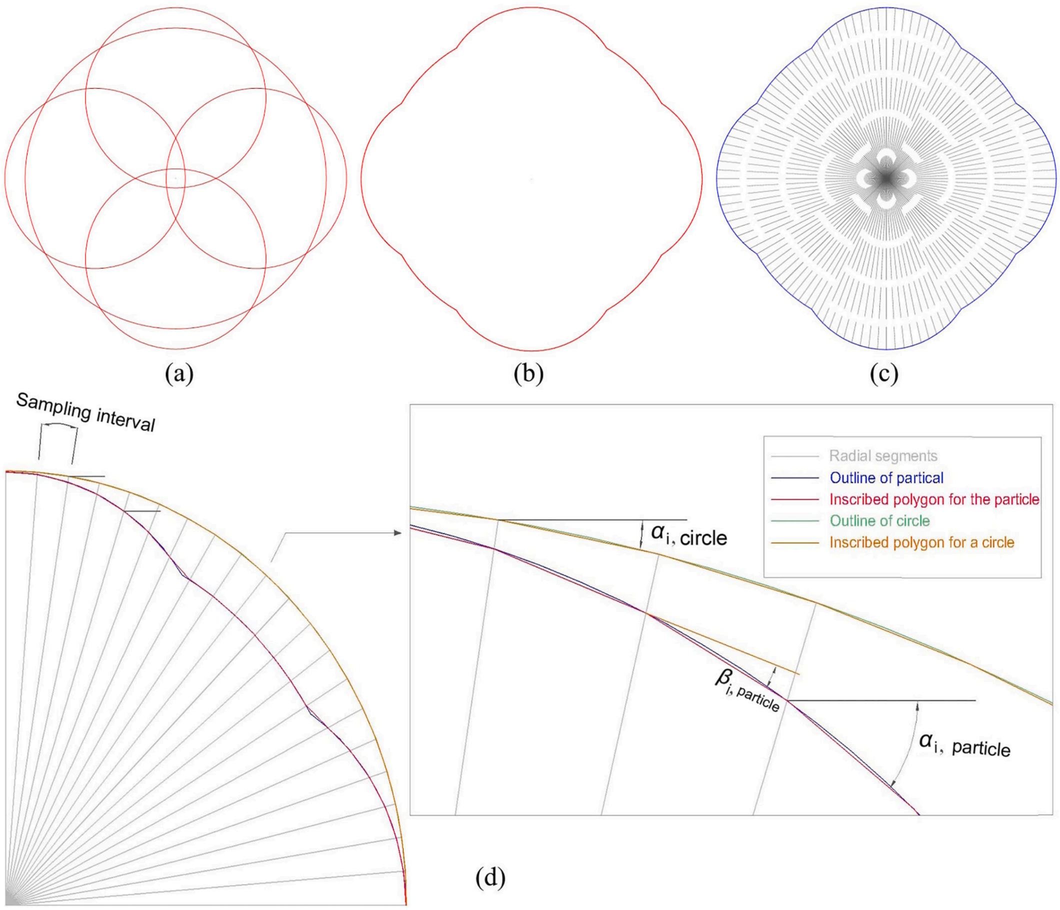


**Fig. 3.** Schematic illustration of the geometric characterization procedure used for calculating the shape factor (SF) and angularity factor (AF): (a) generated particle projection, (b) extracted outer contour, (c) radial sampling intervals used to construct the particle and reference polygons, and (d) definition of the distortion angle ($\alpha_i$) and internal angle ($\beta_i$) employed in the SF and AF calculations.

cut-off between angularity and surface roughness, they also stated that the user can adjust the sampling interval depending on particle geometry, and that smaller sampling intervals are recommended when sharper geometric features need to be captured. Accordingly, a finer angular discretization (N = 120) was adopted in the present study to reduce the possibility of overlooking relatively subtle angularity- and roughness-related features in the particle projections. Radial lines were generated based on the defined angular discretization, and their intersection points with the extracted outer contour were identified. These intersection points were subsequently connected by straight segments to obtain a polygonal approximation of the particle boundary. Using the same angular sampling scheme, a reference polygon representing a flat particle (circle) was constructed at the particle center. Here, the term "flat particle" follows the terminology of Sukumaran and Ashmawy (2001) and denotes the circular reference geometry used for normalization. For each sampling interval $i$, the orientations of the corresponding polygon edges were first evaluated with respect to a fixed horizontal reference, yielding $\alpha_{i,particle}$ for the particle polygon and $\alpha_{i,flat\ particle}$ for the reference polygon. The distortion angle ($\alpha_i$) was then defined as the difference between these two orientation angles, i.e., $\alpha_i = \alpha_{i,particle} - \alpha_{i,flat\ particle}$, which is equivalent to the angle between the corresponding polygon edges and is evaluated from their relative orientations rather than from a local tangent or slope of the smooth contour, as schematically illustrated in Fig. 3(d).

The total magnitude of the distortion angles across all sampling intervals reflects the degree of deviation of the particle projection from a circular shape, and SF is calculated using the following equation:

$$SF = \frac{\sum_{i=1}^{N} \alpha_i}{\sum_{i=1}^{N} \alpha_{i,flat\ particle}} \times 100\% \quad (1)$$

AF parameter is defined in terms of the interior angles ($\beta_i$) of the polygon representing the particle. In a regular circle, the interior angle is 180° for each sampling interval; therefore, the deviation of the particle's interior angles from this value quantitatively expresses the sharpness of the particle's corners, as shown in Fig. 4. To amplify this deviation, the squares of the differences are taken, and AF is calculated as follows:

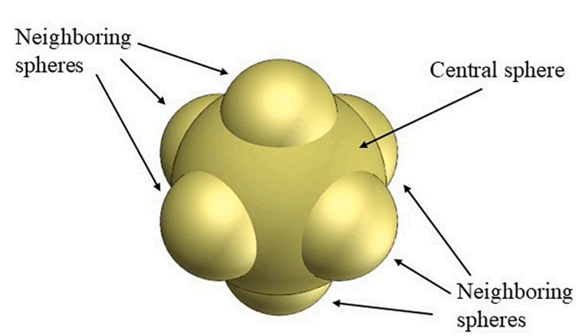


**Fig. 4.** Schematic representation of the particle-generation process and the resulting 3D clumped DEM particles.

$$AF = \frac{\sum_{i=1}^{N} \left(\beta_{i,particle} - 180\right)^2 - \left(360^2/N\right)}{\left(3 \times 180^2\right) - \left(360^2/N\right)} \times 100\% \tag{2}$$

Here, $\left(3 \times 180^2\right)$ in the denominator corresponds to the "cross" form, which has the highest sharpness in the literature, and is used as a normalizing upper bound.

The particle geometries used in this study were designed for research purposes, unlike the natural granular particles typically found in the literature. The particles consist of a central sphere in three dimensions, together with six neighboring spheres symmetrically positioned along the ±x, ±y, and ±z directions. Accordingly, the two-dimensional geometry used for SF and AF calculations corresponds to the x–y projection of the full three-dimensional particle, in which only the four neighboring circles lying in the x–y plane are directly visible. The volume of each particle was kept constant, and its outline was created in AutoCAD. More specifically, the two-dimensional outlines were created in AutoCAD, and the dimensions of the corresponding three-dimensional clumped particles were adjusted to maintain a constant equivalent diameter. Twenty distinct geometric variations with different SF and AF values were obtained by altering the radii of all circles forming the particle and the positions of the neighboring circles. The resulting particle family should therefore be interpreted as an idealized, centrally symmetric clumped geometry set, constructed to enable a controlled comparison of shape effects under consistent numerical conditions.

Since SF and AF are calculated based on a two-dimensional outline, the orientation of the particle in space does not affect these parameters. However, it is known that the random orientation of particles during a confined compression test can alter the packing arrangement and consequently the compressibility. To accurately transfer the SF and AF values calculated from the two-dimensional outer contour to the three-dimensional particles used in DEM analyses, each 2D contour was associated with a corresponding three-dimensional clumped particle composed of one central sphere and six symmetrically positioned neighboring spheres (Fig. 4). In this way, the SF and AF values obtained from the x–y projection were consistently linked to a three-dimensional DEM geometry with the same controlled morphological variation. All 3D particles were generated with constant volume while preserving the controlled morphological characteristics defined in 2D. This approach minimizes orientation-induced variability, ensuring that differences in mechanical response arise predominantly from particle shape rather than initial alignment effects. Because SF and AF were derived from two-dimensional particle projections using a prescribed angular discretization, the resulting values are specific to the adopted projection and sampling framework and should be interpreted accordingly. It should also be noted that the adopted clumped-particle representation provides controlled geometric variation, but does not reproduce the full range of sharp edges, surface roughness, and contact forms that may be encountered in natural granular materials.

Each of the twenty different particle geometries created in this study has been quantitatively defined using SF and AF, whose calculation methods are described above. All particles were designed to have a constant volume; however, a wide morphological diversity, ranging from low irregularity to high angularity, was obtained by systematically varying the radii and positions of the central and neighboring spheres. All designed geometries were transferred to the DEM environment under the same preparation conditions. Therefore, each particle model was filled from the same height using the air-pluviation technique. During the filling stage, the interparticle friction coefficient was set to 0 to ensure equal initial density in all models. After the particles were allowed to rest until their kinetic energy dissipated, the friction coefficient was set to 0.24 to restore the actual mechanical interaction conditions. This ensured that the geometric differences were reflected solely in the numerical results through shape-related effects, eliminating, as far as possible within the adopted DEM framework, any side effects arising from the preparation conditions. The two-dimensional projections of the particle geometries, along with the corresponding SF and AF values, are summarized in Table 2 and serve as the basis for the subsequent compressibility analyses.

### 2.4. Extraction of stress-dependent macro–micro response parameters

In this study, data from confined compression analyses were evaluated to determine compressibility behavior at both macro- and micro-scales. In addition to the primary quantitative indicators, representative contact-scale visualizations were extracted to support the interpretation of micro-scale response trends. In all simulations, the upper loading plate was displaced downward at a constant speed of 2.5 mm/s until the upper plate reaction force reached 51,200 N. For a 143 mm-diameter loading plate, this value corresponds to approximately 3.2 MPa of vertical stress and encompasses all characteristic stress levels (100–3200 kPa) considered in the study.

The vertical stress range of 0.1–3.2 MPa was selected by jointly considering the physical behavior of granular assemblies and the numerical stability requirements of the DEM framework. The lower bound corresponds to the onset of load-bearing contact network formation, while the upper bound enables investigation of high-compression states without inducing particle damage or numerical instability. This stress range, therefore, provides a consistent basis for evaluating the stress-dependent compressibility response as a function of particle shape.

#### 2.4.1. Macro-scale response parameter: tangent constrained modulus (M)

Tangent constrained modulus (M) was adopted to represent compressibility behavior at the macro scale. Six predefined stress levels (100, 200, 400, 800, 1600, and 3200 kPa) were evaluated for each particle model. The tangent modulus was preferred over the secant modulus because it captures the instantaneous material response at specific stress states, thereby allowing a more precise quantification of particle-shape effects in stress-dependent regression analyses.

The stress–strain curves were considered from the point at which the vertical stress reached 0.025 MPa, thereby excluding the initial stage dominated by incomplete contact network formation. Starting from this point, stress-strain curves were obtained using the DEM dataset. To obtain a stable and differentiable representation of the stress–strain response, a second-degree polynomial function was fitted to the curves for all particle models. This functional form captures the nonlinear trend of confined compression while avoiding unnecessary model complexity. The fitted polynomials exhibited excellent agreement with the DEM data, with $R^2$ values ranging from 0.999 to 1.000. Consequently, the derivative-based modulus values ($d\sigma/d\varepsilon$) were evaluated from smooth and numerically stable curve representations. For each predefined stress level, the corresponding strain value was first determined by linear interpolation between the two nearest data points. The fitted polynomial was then differentiated, and the tangent constrained modulus ($M = d\sigma/d\varepsilon$) was evaluated at the interpolated strain value. Subsequently, the polynomial functions were differentiated to calculate the $d\sigma/d\varepsilon$ values, i.e., the tangent-constrained modulus (M), for the strain values corresponding to the relevant stress levels. This method enables the systematic and comparable definition of the stress-dependent compressibility response at the macro scale for each particle model.

#### 2.4.2. Micro-scale response parameter: average coordination number ($\overline{Z}$)

Since the DEM framework enables direct tracking of particle-to-particle contacts, the average coordination number ($\overline{Z}$) was adopted as the primary micro-scale descriptor of contact organization. Altair Engineering Inc, (2022) records the number of contacts associated with each particle at every time step, allowing $\overline{Z}$ to be obtained as a continuous time-dependent variable. Although contact configurations may vary locally, the average coordination number provides a representative measure of the average number of contacts per particle and has been widely used to characterize granular microstructure (Hanley et al.,

**Table 2**
The 2D projection of particle DEM geometries used in the study and calculated SF and AF values.

| Particle No. | View of particle DEM model | SF (–) | AF (–) | Particle No. | View of particle DEM model | SF (–) | AF (–) |
|---|---|---|---|---|---|---|---|
| 1 | 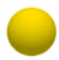 | 0 | 0 | 11 |  | 48.99 | 19.05 |
| 2 |  | 25.59 | 12.62 | 12 |  | 14.70 | 3.99 |
| 3 |  | 9.14 | 3.50 | 13 | 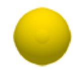 | 3.97 | 0.94 |
| 4 |  | 26.16 | 8.54 | 14 |  | 37.65 | 23.51 |
| 5 |  | 9.17 | 1.54 | 15 |  | 32.76 | 17.13 |
| 6 |  | 44.14 | 15.10 | 16 | 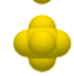 | 46.88 | 17.25 |
| 7 |  | 41.92 | 19.43 | 17 |  | 40.02 | 21.54 |
| 8 |  | 19.76 | 5.87 | 18 |  | 7.10 | 2.11 |
| 9 |  | 34.59 | 19.34 | 19 | 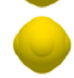 | 12.23 | 2.75 |
| 10 |  | 36.36 | 14.17 | 20 |  | 30.34 | 9.62 |

2014; La Ragione & Jenkins, 2009; Walsh & Tordesillas, 2006; Wensrich, 2014).

For the six predefined vertical stress levels (0.1, 0.2, 0.4, 0.8, 1.6, and 3.2 MPa), the corresponding time steps were first identified from the stress–time series. If the exact stress value coincided with a recorded time step, the associated $\overline{Z}$ value was taken directly. Otherwise, linear interpolation was applied between the two nearest time steps to obtain the coordination number corresponding to the target stress level. This procedure was repeated for all particle models, yielding consistent ($\sigma$, $\overline{Z}$) data pairs at six characteristic stress levels. These stress-dependent coordination number values constitute the micro-scale counterpart of the compressibility response and form the basis for the subsequent multivariate micro–macro analysis.

### 2.4.3. Qualitative contact-scale visualizations: normal-force and normal-overlap patterns

To complement the quantitative micro-scale description provided by $\overline{Z}$, qualitative contact-scale visualizations were also examined for five representative particle shapes. In these visualizations, contact vectors were colored by the magnitude of the normal contact force, and contact points were separately colored by the magnitude of the normal overlap. The normal-force-colored contact vectors were used to visualize the distribution and intensity of force transmission within the contact network, whereas the normal-overlap maps were used to qualitatively assess the distribution of local contact deformation among interacting particles. Because displaying all contacts within the full specimen would lead to severe visual overlaps and make interpretation difficult, the visualizations were restricted to a central slice extracted from the specimen. This slice was selected from the model center and assigned a thickness equal to the equivalent particle diameter (10 mm) to clearly visualize both contact-force and normal-overlap patterns. Several alternative slice thicknesses were also examined, and the clearest representation was found to be obtained when the slice thickness was chosen equal to the equivalent particle diameter. These visualizations were evaluated at the time step closest to a vertical stress of 0.8 MPa, thereby enabling direct comparison of the selected particle shapes at the same stress level and supporting the interpretation of shape-dependent changes in contact organization, force transmission, and local overlap patterns. The stress level of 0.8 MPa was selected because it represents the intermediate range of the investigated stress interval and was considered suitable for observing the general contact-scale behavior without being restricted to either the initial low-stress rearrangement regime or the most highly compressed state. In addition, the color-scale intervals used for both normal-force and normal-overlap visualizations were kept constant across all representative particle shapes to enable direct visual comparison. The selected ranges were determined through preliminary visualization trials and were chosen to maximize the clarity and interpretability of shape-related differences in contact-force and overlap distributions. The same slice definition and color scale settings were used for all five representative particle shapes to ensure consistency in the visual comparison. These visualizations were not used as primary regression variables, but rather as qualitative contact-scale evidence to complement the macro- and micro-scale indicators adopted in the study.

### 2.4.4. Quantitative contact-scale statistics

To strengthen the micro-scale interpretation beyond qualitative contact visualization, additional quantitative contact-scale statistics were extracted from the DEM results for the selected representative particle models. The same five representative geometries used in the contact-scale visualizations were considered, namely Model 1, Model 12, Model 2, Model 9, and Model 11, arranged in order of increasing SF. This ordering was adopted to maintain consistency with the normal-force and normal-overlap visual comparisons at 0.8 MPa. Unlike the visualizations, which were restricted to a central slice for clarity, the quantitative contact-scale statistics were calculated from all active contacts in the full specimen.

The contact-force-based analyses were performed at four vertical stress levels: 0.1, 0.4, 0.8, and 3.2 MPa. These stress levels were selected to represent the low-stress rearrangement regime, the onset of clearer shape-dependent response, a representative intermediate stress state, and the upper-bound stress condition of the simulations, respectively.

The detailed coordination-number distribution and normal-overlap statistics were evaluated at 0.8 MPa, which is the same representative stress level used for the qualitative contact-force and normal-overlap visualizations.

For each representative particle model and selected vertical stress level, the mean normal contact force ($\overline{F_n}$) was calculated using all active contacts in the full specimen as follows:

$$\overline{F_n} = \frac{1}{N_c}\sum_{c=1}^{N_c} F_{n,c} \tag{3}$$

where $F_{n,c}$ is the normal force at contact $c$, and $N_c$ is the total number of active contacts. To evaluate how the mean contact force scales with the applied vertical stress, the relationship between $\overline{F_n}$ and vertical stress ($\sigma_v$) was approximated for each representative particle model using a zero-intercept linear fit:

$$\overline{F_n} = k_F \sigma_v \tag{4}$$

where $k_F$ is the slope of the fitted relationship and represents the mean normal contact force mobilized per unit vertical stress. Since $\overline{F_n}$ is expressed in N and $\sigma_v$ in MPa, the unit of $k_F$ is N/MPa. This parameter was used as a stress-normalized contact-force coefficient, allowing the mean contact-force response of different particle shapes to be compared after reducing the direct influence of vertical stress.

A binary weak–strong contact classification was also performed using the normal contact force. For each particle model and stress level, the normalized normal contact force was defined as shown in Equation (5).

$$f_n^* = \frac{F_{n,c}}{\overline{F_n}} \tag{5}$$

Contacts satisfying $f_n^* < 1$, or equivalently $F_{n,c} < \overline{F_n}$, were classified as weak contacts, whereas contacts satisfying $f_n^* \geq 1$ were classified as strong contacts. The classification threshold was therefore defined separately for each particle model and stress level using the corresponding mean normal contact force. The weak-contact percentage ($WCP$) was calculated as:

$$WCP = \frac{N\left(f_n^* < 1\right)}{N_c} \times 100 \tag{6}$$

where $N\left(f_n^* < 1\right)$ is the number of contacts with below-average normal force. This parameter was used to quantify how the fraction of weak contacts changes with particle shape and vertical stress.

In addition to the average coordination number $\overline{Z}$, the particle-level coordination-number distribution was evaluated to examine how contacts were distributed among individual particles. For each selected particle model, the coordination number of each particle ($Z_i$) was obtained at the time step corresponding to 0.8 MPa. The fraction of particles having a given coordination number ($Z = j$) was calculated as:

$$P(Z = j) = \frac{N(Z_i = j)}{N_p} \tag{7}$$

where $N(Z_i = j)$ is the number of particles with coordination number $j$, and $N_p$ is the total number of particles in the assembly. This distribution was used to determine whether the increase in the average coordination number reflected a general shift of the particle population toward higher coordination states or was driven solely by a limited number of highly coordinated particles.

Quantitative normal-overlap statistics were calculated to support the interpretation of local contact deformation. These statistics were extracted from all active contacts in the full specimen at 0.8 MPa, corresponding to the stress level used in the normal-overlap visualizations. The normal overlap ($\delta_n$) at each active contact was first normalized by the equivalent particle diameter ($d_{eq}$) as shown in Equation (8).

$$\delta_n^* = \frac{\delta_n}{d_{eq}} \tag{8}$$

Since all particles were generated with equal volume, $d_{eq}$ was constant for all particle geometries. To examine the relative distribution of local contact deformation ($r_\delta$) within each particle model, the normalized overlap of each contact was further divided by the mean normalized overlap of the corresponding model:

$$r_\delta = \frac{\delta_n^*}{\overline{\delta_n^*}} \tag{9}$$

where $\overline{\delta_n^*}$ is the mean normalized normal overlap for the relevant particle model. The fraction of contacts falling within each relative-overlap interval was then calculated to obtain the relative overlap distribution.

In addition, the mean normalized normal overlap, the 95th percentile of normalized normal overlap $\left(P_{95}\left(\delta_n^*\right)\right)$ and the coefficient of variation of normalized normal overlap ($CV_\delta$) were calculated as summary descriptors. The coefficient of variation was defined as:

$$CV_\delta = \frac{SD\left(\delta_n^*\right)}{\overline{\delta_n^*}} \tag{10}$$

where $SD\left(\delta_n^*\right)$ is the standard deviation of the normalized overlap of the contacts. The 95th percentile represents the normalized overlap value below which 95% of the contacts fall, whereas $CV_\delta$ characterizes the relative dispersion of local contact deformation within each particle model. These overlap statistics were used to provide a quantitative counterpart to the normal-overlap visualizations and to assess how contact deformation is distributed among active contacts for different particle geometries.

### 2.5. Regression-based modeling of macro–micro mechanical behavior

This study aims to quantitatively evaluate the shape-related effect of particle shape on the compressibility behavior of granular materials. The macro-scale tangent modulus (M) and micro-scale average coordination number ($\overline{Z}$) were treated as dependent variables and analyzed using separate regression models. All statistical analyses were performed using SPSS Statistics (2022).

Before establishing the regression models, the relationships between the independent variables were evaluated using Pearson correlation coefficients (Pearson, 1896). This preliminary analysis revealed a strong linear relationship between SF and AF parameters in the dataset used in this study ($r > 0.9$). Given the high correlation, multicollinearity was expected to compromise coefficient stability; therefore, only SF was retained as the independent variable in the regression models. Accordingly, SF was treated as the principal particle-shape descriptor in the subsequent regression analyses.

In granular material mechanics, the observed macro- and micro-scale responses ($M$ and $\overline{Z}$) result from the combined effect of two fundamental parameters: particle shape and stress level. However, macro- and micro-scale responses are inherently stress-dependent, which may obscure the contribution of particle shape, particularly at lower stress levels. Therefore, a methodological separation of stress and shape effects was required prior to regression modeling. This subsection explains how the stress component was isolated and how normalized shape indicators were derived. To separate the stress-dependent component of macro- and micro-scale responses, $M - \sigma$ and $\overline{Z} - \sigma$ relationships were first examined using a log–log transformation to validate the power law relationship in $P \propto \sigma^\alpha$ form, commonly used in the literature. This step was conducted to quantify the dominant stress-scaling behavior of the macro- and micro-scale parameters prior to shape normalization. The power-law relationship is linearized using the natural logarithm (ln) transformation, as shown in Equation (11).

$$\ln(P) = \ln(C) + \alpha \times \ln(\sigma) \quad (11)$$

Here, $P$ represents M or Z; $C$ represents the scaling coefficient in the original power law form. The slope coefficient ($\alpha$) obtained from this regression analysis quantitatively captures the dominant stress-scaling behavior of the relevant parameter in the DEM-simulation data.

The slope coefficients obtained from these log–log regressions ($\alpha_M$ for the modulus and $\alpha_Z$ for the coordination number) quantify the dominant stress-scaling behavior of each parameter. Using the $\alpha_M$ and $\alpha_Z$ stress exponents determined by the log–log transformation, the tangent modulus and coordination number were normalized to obtain comparative descriptors $M_n$ and $Z_n$. This transformation is a methodological step aimed at revealing the comparable shape-related effect of particle shape by reducing the dominant stress-scaling component from data obtained at different stress levels:

$$M_n = \frac{M}{\sigma^{\alpha_M}} \quad (12)$$

$$Z_n = \frac{\overline{Z}}{\sigma^{\alpha_Z}} \quad (13)$$

Following the acquisition of stress-normalized macro- and micro-responses, second-degree polynomial multiple regression models were created to capture the nonlinear effects of particle shape. The functional forms used for $M_n$ and $Z_n$ are shown in Equations (14) and (15), respectively.

$$M_n = \beta_0 + \beta_1 SF + \beta_2 SF^2 + \varepsilon_M \quad (14)$$

$$Z_n = \gamma_0 + \gamma_1 SF + \gamma_2 SF^2 + \varepsilon_Z \quad (15)$$

Here, $\beta_i$ and $\gamma_i$ represent the regression coefficients, while $\varepsilon_M$ and $\varepsilon_Z$ represent the model error terms. The statistical significance of the regression coefficients was assessed at the $p < 0.05$ level. These regression models were adopted as empirical comparative tools for describing systematic trends in the normalized response variables within the analyzed particle family, rather than as universal constitutive relationships.

In addition to the regression models developed for the stress-normalized macro- and micro-scale response indicators, the contact-force coefficient ($k_F$) was also related to SF using a second-order polynomial expression:

$$k_F = a_F SF^2 + b_F SF + c_F \quad (16)$$

where $a_F$, $b_F$, and $c_F$ are regression coefficients. Since $k_F$ was obtained as the slope of the zero-intercept $\overline{F_n}$–$\sigma_v$ relationship, this expression represents the shape-dependent contact-force response after reducing the direct influence of vertical stress. Similar to the other regression relationships, this equation was used as a descriptive relationship for the representative particle models considered in the contact-scale analysis, rather than as a general predictive law.

To evaluate the validity of the primary regression models, standard regression assumptions were tested. Unstandardized residuals were computed for the macro- and micro-scale regression models, and their normality was assessed using the Shapiro–Wilk test (Shapiro & Wilk, 1965). Residual distributions were further evaluated using Q–Q plots, histograms, and skewness–kurtosis statistics. Homoscedasticity was examined by inspecting residuals versus predicted values. Model fit was assessed using $R^2$ and adjusted $R^2$ values. The adequacy of the sample size was confirmed through a post-hoc power analysis based on the Cohen approach (Cohen, 1992). Taken together, these procedures provide a statistically consistent basis for evaluating nonlinear effects of particle shape on stress-normalized macro- and micro-scale response descriptors adopted in this study.

The $k_F$–SF relationship was treated separately as a descriptive contact-scale relationship derived from the five representative particle models selected for detailed contact analysis. Therefore, it was primarily evaluated in terms of its coefficient of determination and its physical consistency with the contact-force trends, rather than being subjected to the same regression-diagnostic procedure applied to the primary macro- and micro-scale models. In addition to the SF-based relationships, supplementary micro–macro associations were examined by relating the contact-scale indicators $k_F$ and $\overline{\delta_n^*}$ to the normalized tangent constrained modulus ($M_n$) for the five representative particle models. These associations were used only to support the micro–macro interpretation and were not treated as independent predictive regression models.

It should be noted, however, that the present regression analysis was performed on a controlled DEM dataset generated under a single modeling configuration. The adopted particle count was considered sufficient for the present comparative analyses, although additional sensitivity studies with larger assemblies would be valuable for a more comprehensive assessment of the influence of specimen size and boundary effects. Likewise, variability associated with repeated realizations of the initial packing arrangement was not explicitly quantified in the present study. Accordingly, the resulting relationships should be interpreted as comparative empirical trends within the analyzed particle family rather than as fully uncertainty-quantified predictive laws.

## 3. Results

### 3.1. Macro-scale compressibility response: stress–tangent constrained modulus relationship

The stress–strain curves obtained from the confined compression analyses were fitted using polynomial functions, as described in the Methods section. The tangent-constrained modulus (M) was subsequently calculated by differentiating the fitted curves, allowing the modulus to be evaluated continuously as a function of vertical stress. In this manner, the stress-modulus (M–σ) relationship was obtained as a continuous response relationship. Fig. 5 presents these stress-dependent response descriptors together, with the tangent constrained modulus representing the macro-scale response and the average coordination number representing the micro-scale contact-network response. In particular, Fig. 5a presents representative M–σ curves for four particle shapes, illustrating the evolution of macro-scale stiffness with increasing stress and highlighting the influence of particle shape on compressibility.

The M–σ curves were obtained for four representative particle models—zero SF (particle 1), low SF (particle 5), high SF (particle 10), and maximum SF (particle 11)—selected from the twenty geometries listed in Table 2. A comparison of these curves in Fig. 5a indicates that the macro-scale compressibility response depends on both the particle's SF value and the applied vertical stress level. At low stress levels, all models exhibit very similar modulus values, and no consistent trend between particle shape and stiffness is observed in this range. The response in this regime appears to be governed primarily by particle rearrangement and void closure processes, which limit the manifestation of shape-related effects. Within this low-stress domain, particle model 11 (maximum SF) shows relatively higher M values, whereas particle model 10 exhibits comparatively lower stiffness, with particle model 5 displaying intermediate behavior.

As the applied stress increases, the tangent-constrained modulus increases across all particle models, indicating a progressively stiffer macro-scale response. In this higher-stress regime, differences in modulus between particle shapes become more pronounced. Particle model 10, which exhibits relatively low stiffness at low stress levels, attains the highest modulus values at medium and high stresses compared to the other models. This behavior suggests that particle shape effects become increasingly influential as contact stabilization reaches a sufficient level.

In contrast, particle model 11 (maximum SF) does not consistently

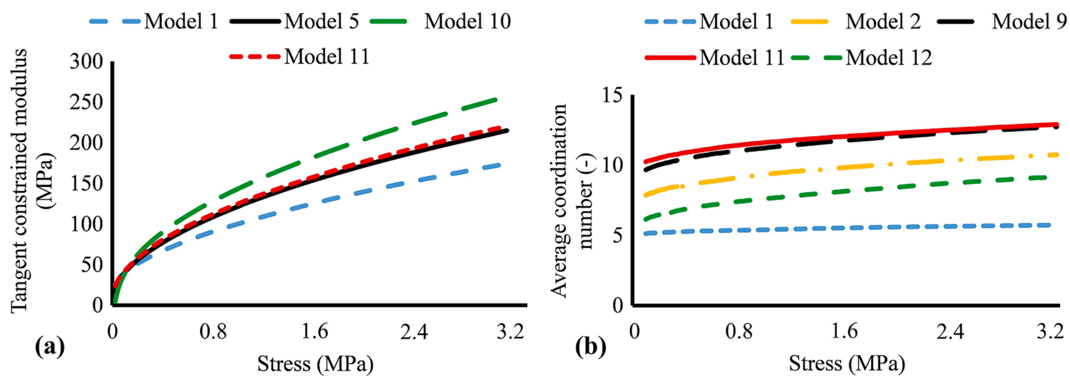


**Fig. 5.** Variation of the macro- and micro-scale response descriptors with vertical stress for different particle shapes: (a) tangent constrained modulus, and (b) average coordination number.

yield the highest stiffness at elevated stress levels. Although this model shows comparatively higher modulus values in the low-stress regime, its stiffness remains lower than that of model 10 at higher stresses. These observations indicate that increased geometric irregularity does not necessarily result in higher stiffness across all stress levels. Overall, the stiffness–shape relationship exhibits a non-monotonic trend, with shape-related effects depending on the applied stress level.

These results indicate that the influence of particle shape on macro-scale compressibility becomes more apparent beyond a certain stress level. At low stresses, the response appears to be dominated by particle rearrangement processes, which limit the clear manifestation of shape-related effects. Accordingly, the stress-normalization procedure introduced in this study provides a useful basis for comparative analysis of shape-related trends after reducing the dominant influence of stress on the compressibility response.

### *3.2. Micro-scale compressibility response: stress – average coordination number relationship*

To examine the evolution of the average coordination number ($\overline{Z}$) with vertical stress ($\sigma$) for particles with different shapes, five representative models (Model 1: SF = 0, Model 2: SF = 25.6, Model 9: SF = 34.59, Model 11: SF = 48.99, and Model 12: SF = 14.7) were selected from the twenty particle geometries listed in Table 2. The resulting $\overline{Z}$–$\sigma$ relationships for these models are presented in Fig. 5b. As shown in Fig. 5b, the average coordination number increases with increasing stress for all particle shapes; however, the magnitude of this increase remains relatively limited over the investigated stress range. When the vertical stress increases from 0.1 MPa to 3.2 MPa, variations in $\overline{Z}$ are modest compared to the pronounced changes observed in the macro-scale modulus response. Accordingly, the $\overline{Z}$–$\sigma$ curves exhibit low slopes for all particle geometries, indicating a weak stress dependence of the average coordination number within the examined range. These results suggest that, although stress contributes to contact network evolution, the observed differences in coordination number within the investigated range are more closely related to particle shape than to stress level.

A comparison of the five representative models indicates that particle shape consistently influences the average coordination number across the investigated stress range. Model 1, consisting of spherical particles, exhibits the lowest coordination number at all stress levels, whereas particles with more irregular geometries systematically display higher average coordination numbers. This relative ranking is preserved at low, medium, and high stresses, suggesting that contact topology is strongly associated with particle shape rather than with stress level alone.

As the SF value increases, the average coordination number also increases; however, the incremental gain in $\overline{Z}$ gradually diminishes. In particular, Models 9 and 11 exhibit very similar coordination numbers despite their differences in SF, suggesting that saturation has begun. This observation implies that increasing particle irregularity enhances contact formation up to a certain level, beyond which additional geometric complexity results in only a limited increase in coordination number.

Overall, these results show that particle shape has a more persistent influence on the coordination number than stress within the examined stress range. The relatively weak stress dependence of $\overline{Z}$ suggests that this micro-scale descriptor may provide a useful basis for stress-normalized analyses of shape effects.

### *3.3. Contact-scale force and overlap patterns in representative particle shapes*

To provide qualitative support for the micro-scale interpretation, contact-scale visualizations were examined for the same five representative particle models used in Section 3.2, namely Model 1, Model 12, Model 2, Model 9, and Model 11, arranged in order of increasing SF. This consistent selection and ordering were adopted to facilitate direct comparison between different indicators of micro-scale behavior. The visualizations were extracted from the time step corresponding most closely to a vertical stress of 0.8 MPa, so that all particle shapes could be evaluated under the same stress level. In addition, the color scales used for both the normal contact force and the normal overlap were kept constant across all representative particle models, thereby enabling direct visual comparison across particle shapes. For clarity, the corresponding color legends are presented only in panel (a) of each figure.

Fig. 6 presents the contact vectors colored by the magnitude of the normal contact force, with white, red, and black indicating increasing force magnitude. A qualitative comparison of these contact-force distributions indicates that the number and spatial density of contact vectors increase with increasing SF. At the same time, the color distribution suggests that the normal force per contact decreases with increasing SF. Since all representative particle models were evaluated at the same stress level, this observation is consistent with the interpretation that increasing the SF promotes the formation of more contacts, in agreement with the increase in the average coordination number observed in Section 3.2. Consequently, the transmitted load appears to be distributed over a denser contact network, thereby reducing the force carried per contact point. However, consistent with the trend already observed in Fig. 5b, the incremental micro-scale influence of the SF appears to diminish beyond a certain level. This attenuation is also visible in the contact-force visualizations, where the differences between the higher-SF particle shapes become less pronounced.

Similarly, Fig. 7 shows the contact points colored by the magnitude of the normal overlap, with white, dark red, and black indicating increasing overlap values. These visualizations show that the number of overlapping points increases with increasing SF, while the color

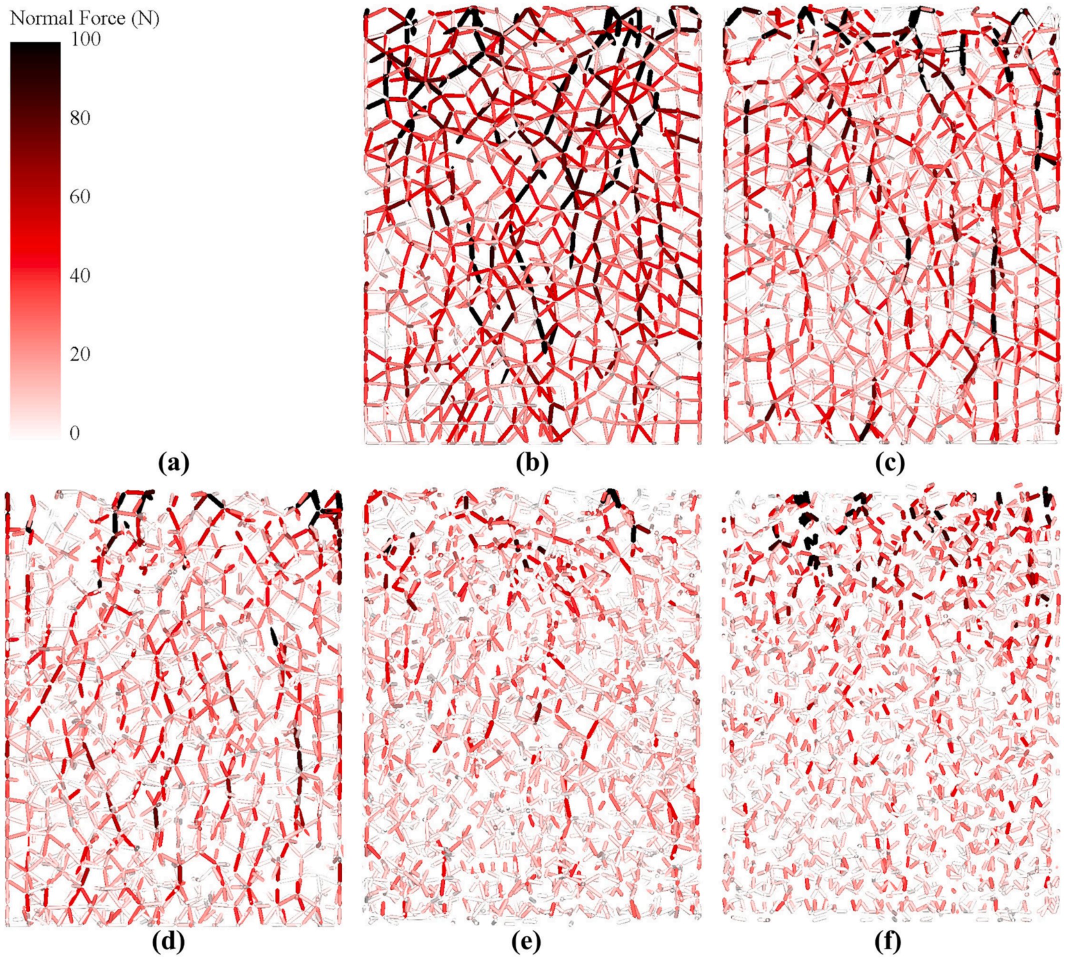


**Fig. 6.** Distribution of contact vectors colored by normal contact force magnitude for five representative particle shapes at a vertical stress level of 0.8 MPa: (a) common color legend, (b) Model 1, (c) Model 12, (d) Model 2, (e) Model 9, and (f) Model 11. The particle models are arranged in order of increasing SF values.

distribution suggests that the magnitude of overlap per contact becomes less concentrated. In other words, although a greater number of contact points is mobilized in particles with higher SF, the overlap per contact appears to be lower on average. This pattern is qualitatively consistent with the force-distribution observations and suggests that local contact deformation is distributed among a larger number of contacts in the more irregular particle assemblies. As in the coordination-number response, the visual differences in overlap distribution also become less marked at higher SF, suggesting a progressive reduction in the incremental influence of further shape irregularity on the micro-scale response.

Overall, the contact-force and overlap visualizations support the interpretation that increasing particle-shape irregularity is associated with denser contact organization, broader force transmission, and a more distributed pattern of local overlap under the same applied stress level. At the same time, the observed visual convergence at higher SF is consistent with the diminishing incremental increase in average coordination number identified in Section 3.2. Although these observations are qualitative and limited to representative cases, they provide contact-scale evidence consistent with the trends identified from the coordination number analyses.

### 3.4. Quantitative contact-scale statistics

To complement the qualitative contact-force and normal-overlap visualizations presented in Figs. 6 and 7, additional quantitative contact-scale statistics were evaluated for the same representative particle models. These analyses were performed using all active contacts in the full specimen, rather than only the central slice used for visualization. Therefore, the results provide a quantitative basis for interpreting the contact-scale mechanisms underlying the macro- and micro-scale trends discussed in the preceding sections.

#### 3.4.1. Mean normal contact force scaling and shape dependence of $k_F$

Before defining the stress-normalized contact-force coefficient, the mean normal contact force was first examined as a function of vertical stress for each representative particle model. As shown in Fig. 8a–e, the mean normal contact force increases almost linearly with vertical stress for all five representative particle models. The zero-intercept linear fits yielded coefficients of determination greater than 0.99 for all representative models, indicating that the stress dependence of the mean normal contact force can be consistently represented by a single slope parameter. Accordingly, the slope of each fitted line was defined as $k_F$, representing the mean normal contact force mobilized per unit vertical stress.

The obtained $k_F$ values differ considerably among the particle geometries, indicating that particle shape affects how the externally applied vertical stress is distributed among contacts. To evaluate this shape dependence, the resulting $k_F$ values were plotted against SF, as shown in Fig. 8f. The spherical model exhibits the highest $k_F$, whereas the non-spherical models generally show lower values. This indicates that, for a given vertical stress, the mean force carried by each contact tends to decrease as the contact network becomes denser in the non-spherical particle assemblies.

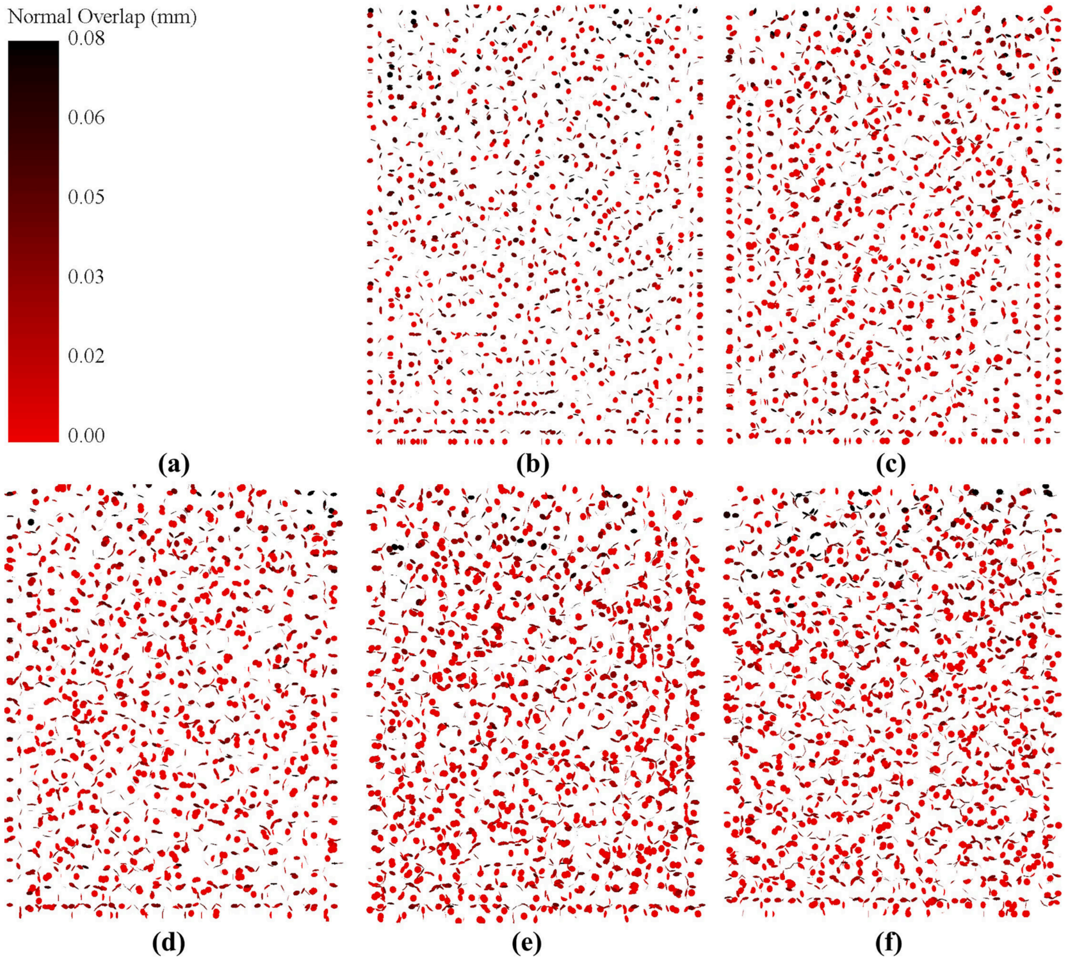


**Fig. 7.** Distribution of contact points colored by normal overlap magnitude for five representative particle shapes at a vertical stress level of 0.8 MPa: (a) common color legend, (b) Model 1, (c) Model 12, (d) Model 2, (e) Model 9, and (f) Model 11. The particle models are arranged in order of increasing SF.

The variation of $k_F$ with SF is nonlinear and can be described by the following second-order expression:

$$k_F = 0.016SF^2 - 1.25SF + 40.46 \quad (17)$$

with $R^2 > 0.99$. This relationship indicates that $k_F$ decreases sharply from the spherical reference toward the intermediate SF range, suggesting that the initial increase in particle-shape irregularity reduces the mean contact force mobilized per unit vertical stress. However, the decreasing trend becomes weaker at higher SF values, and a slight upward tendency is observed near the upper end of the investigated SF range. Therefore, the $k_F$ - SF relationship should not be interpreted as a continuously monotonic decrease. Rather, it indicates a nonlinear, saturation-like response in which the influence of shape irregularity on contact-force redistribution becomes less pronounced at higher SF values.

### 3.4.2. Weak-contact percentage under different predefined vertical stresses

Fig. 9 shows the weak-contact percentage as a function of SF at selected vertical stress levels. In this analysis, weak contacts were defined relative to the mean normal contact force calculated separately for each particle model and vertical stress level; that is, contacts satisfying $F_n < \overline{F_n}$ were classified as weak contacts. At 0.1 MPa, the relationship between SF and weak-contact percentage is comparatively scattered, with a lower coefficient of determination. This behavior is consistent with the low-stress regime identified in the macro-scale response, where particle rearrangement and incomplete contact-network stabilization obscure systematic shape-related trends.

As vertical stress increases to 0.4 MPa and above, the relationship between SF and weak-contact percentage becomes more consistent, with $R^2$ values exceeding 0.95 at higher stress levels. This indicates that once the contact network becomes sufficiently developed, particle shape has a clearer influence on the partitioning of contacts into weak and strong force-carrying groups. In addition, the SF value corresponding to the maximum weak-contact percentage tends to shift toward lower SF values as the vertical stress increases. This suggests that the force-partitioning response becomes increasingly sensitive to particle shape as the assembly transitions from a rearrangement-dominated regime to a more developed load-bearing state.

### 3.4.3. Coordination-number distribution at 0.8 MPa

The particle-level coordination-number distributions at 0.8 MPa are presented in Fig. 10. The distribution for the spherical model is concentrated over a narrower range of lower coordination numbers. As SF increases, the distribution progressively shifts toward higher coordination numbers and becomes broader. At the same time, the peak particle fraction decreases, indicating that the contact states are distributed over a wider range of coordination numbers.

This result shows that the increase in average coordination number reported in Section 3.2 is not only a change in a single mean value. Rather, it reflects a broader redistribution of particle-level contact states toward higher coordination numbers. This behavior supports the interpretation that increasing SF promotes the formation of a denser and more heterogeneous contact network.

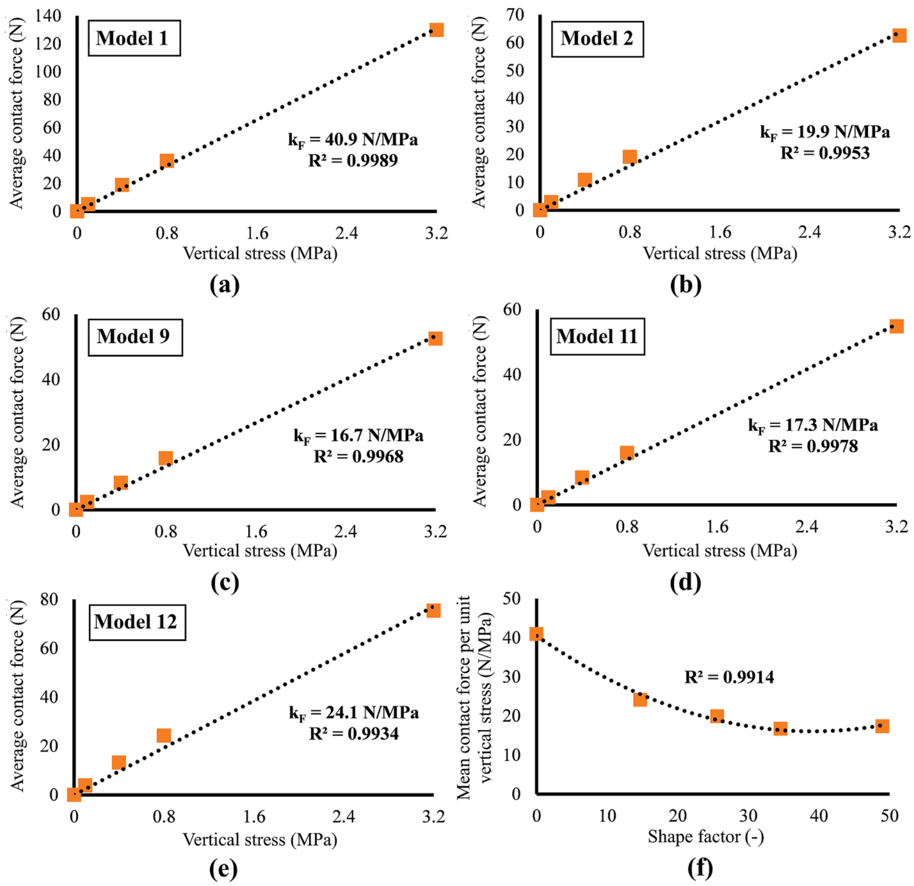


**Fig. 8.** Evaluation of the mean normal contact-force response for the five representative particle models: (a–e) mean normal contact force–vertical stress relationships, and (f) variation of the stress-normalized mean contact-force coefficient ($k_F$) with shape factor (SF).

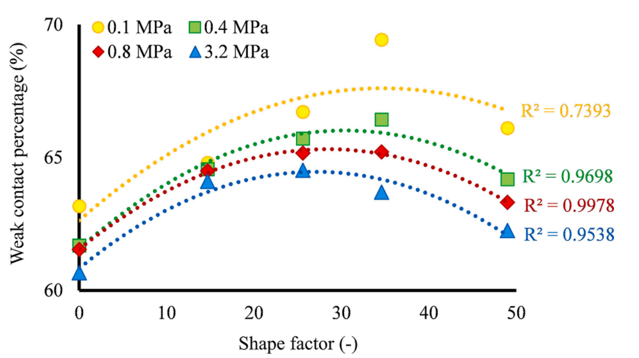


**Fig. 9.** Weak-contact percentage as a function of SF at selected vertical stress levels. The weak-contact percentage was calculated based on contacts satisfying $F_n < \overline{F_n}$ for each particle model and stress level.

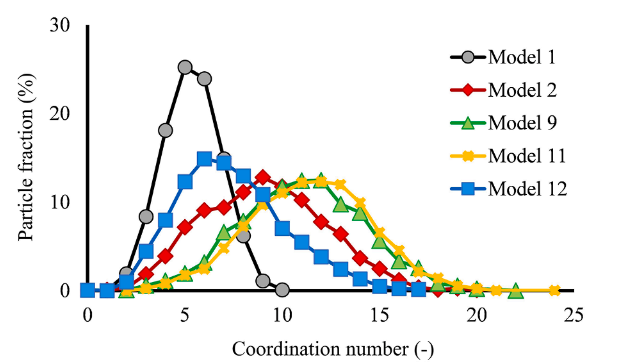


**Fig. 10.** Particle-level coordination-number distribution at a vertical stress level of 0.8 MPa for the five representative particle models arranged in order of increasing SF. The particle fraction was calculated as the ratio of particles with a given coordination number to the total number of particles in the assembly.

### 3.4.4. Normal-overlap statistics at 0.8 MPa

Fig. 11 presents the quantitative normal-overlap statistics at 0.8 MPa. In Fig. 11(a), the relative normalized overlap distribution is shown using $r_\delta = \delta_n^*/\overline{\delta_n^*}$, where $\delta_n^*$ is the normal overlap normalized by the equivalent particle diameter. This distribution provides a quantitative counterpart to the normal-overlap visualization in Fig. 7. The cumulative relative-overlap curves exhibit broadly similar shapes across the selected particle geometries, indicating that the general shape of the overlap distribution is not strongly altered by particle geometry when each model is normalized by its own mean overlap. However, the maximum relative normal-overlap range first increases with SF and then decreases at higher SF values, suggesting a non-monotonic change in the upper tail of the relative overlap distribution.

The summary descriptors in Fig. 11(b–d) shows the variation of the mean normalized normal overlap, the 95th percentile normalized normal overlap, and the coefficient of variation of normalized normal overlap with SF. All three descriptors exhibit a nonlinear shape-dependent trend. A marked reduction is observed from the spherical reference toward irregular particle shapes, followed by a plateau-like response and a slight tendency toward increase near the upper end of the investigated SF range. This indicates that local contact deformation decreases rapidly at first as the contact network becomes more distributed, but its sensitivity to further increases in SF weakens at higher

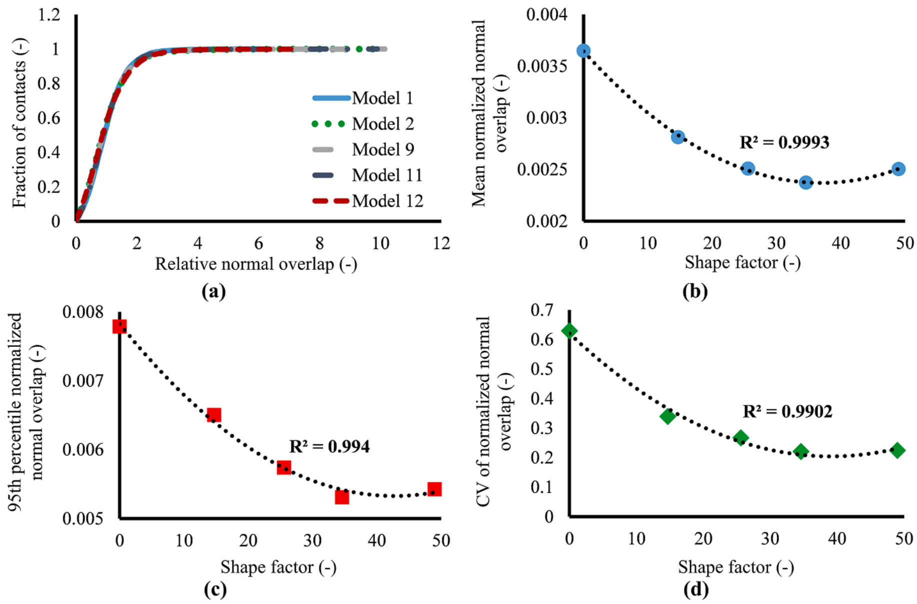


**Fig. 11.** Quantitative normal-overlap statistics at 0.8 MPa for the five representative particle models: (a) cumulative distribution of relative normalized normal overlap, (b) mean normalized normal overlap, (c) 95th percentile normalized normal overlap, and (d) coefficient of variation of normalized normal overlap. The normalized normal overlap is defined as $\delta_n^* = \delta_n/d_{eq}$, and the relative normalized overlap in panel (a) is defined as $r_\delta = \delta_n^*/\overline{\delta_n^*}$.

irregularity levels. The coefficient of variation further shows that particle shape affects not only the average level and upper-tail magnitude of local contact deformation, but also the relative dispersion of overlap values among active contacts.

Taken together, the quantitative contact-scale analyses presented in Section 3.4 show that particle shape affects the contact-scale response through multiple mechanisms. Increasing SF modifies the weak-contact percentage, broadens the coordination-number distribution, reduces the mean normal force mobilized per unit vertical stress over much of the investigated shape range, and alters the distribution of local overlap.

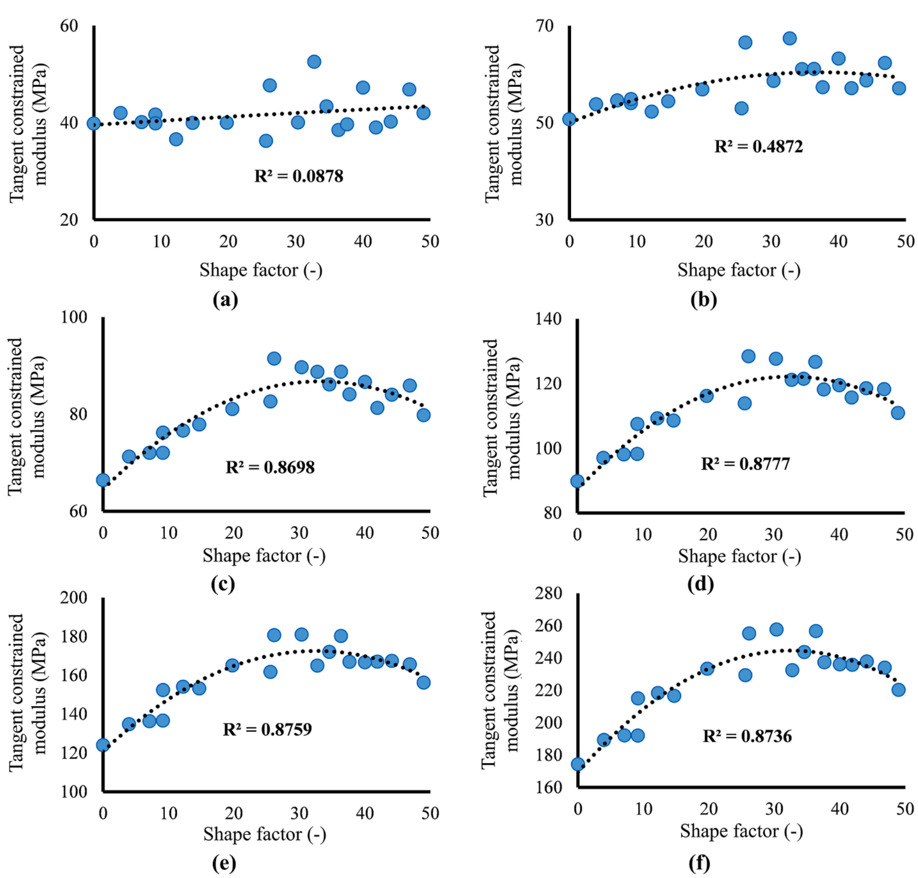


**Fig. 12.** The M–SF relationship for predefined vertical stresses, (a) 0.1 MPa, (b) 0.2 MPa, (c) 0.4 MPa, (d) 0.8 MPa, (e) 1.6 MPa, (f) 3.2 MPa.

These findings indicate that the micro-scale influence of particle shape cannot be represented solely by the average coordination number, but also involves force partitioning and contact-scale deformation characteristics.

### 3.5. Macro-scale shape effect under predefined stress levels

The relationship between M and SF was evaluated separately at six predefined vertical stress levels to determine how particle shape affects macro-scale stiffness under different stress conditions. As explained in the Methodology section, each M value was obtained by interpolating the strain corresponding to a constant vertical stress and calculating the derivative of the fitted stress–strain function at that point. Therefore, the modulus values shown in Fig. 12 are not raw measurement points, but derivative-based representative values obtained in a comparable form at the same vertical stress levels.

The relationship between SF and M at the 0.1 and 0.2 MPa stress levels, as shown in Fig. 12(a) and (b), remains relatively unclear. Models with different SF values produced very similar M values in this low-stress regime; the curves remained generally horizontal, and no well-defined trend emerged from the data. This situation indicates that at low stress levels, the stiffness response does not yet show a clear systematic dependence on particle shape and is primarily governed by early-stage deformation mechanisms, such as particle rearrangement and void closure. This interpretation is also consistent with the contact-scale results presented in Section 3.4, where the weak-contact percentage exhibited a less regular relationship with SF at the lowest stress level.

When the vertical stress level reaches 0.4 MPa (Fig. 12c), a clearer shape-dependent trend becomes observable in the M–SF curves. Beginning at this level, the effect of different shape morphologies on stiffness becomes more apparent. When examining the graphs obtained for stresses of 0.8, 1.6, and 3.2 MPa (Fig. 12d–f), it is seen that the form of the M–SF relationship continues to maintain the character that emerged at 0.4 MPa. The $R^2$ values are quite similar across these stress levels, indicating that the strength of the relationship does not change significantly once the contact network has developed sufficiently.

When these findings are evaluated together, it becomes evident that the effect of particle shape on macro-scale stiffness emerges only after a threshold stress is exceeded. Since the shape effect is masked by mechanical behavior at 0.1 and 0.2 MPa, the M–SF relationships at low stresses are less informative about shape-related trends. In contrast, the progressive emergence of the shape effect at stresses above 0.4 MPa demonstrates that stress normalization and exponential calculations based solely on this stress range are mechanically justified within the adopted framework. More broadly, these results support the need for stress normalization in order to compare shape-related trends after reducing the dominant influence of vertical stress.

### 3.6. Micro-scale shape effect under predefined stress levels

The relationship between $\overline{Z}$ and SF was evaluated separately at six predefined vertical stress levels to examine the average number of interparticle contacts as a micro-scale response to stress. The $\overline{Z}$–SF curves presented in Fig. 13 show that the response of the contact structure to particle geometry exhibits a character significantly different from that of macro-scale stiffness.

At all stress levels, $\overline{Z}$ increases systematically with SF, and the curves are quite similar in form. It is observed that even at the lowest stress level of 0.1 MPa, spherical particles produce the lowest coordination numbers, while particles with higher SF values have a denser contact network. At the 0.2, 0.4, and 0.8 MPa levels, the general shape of the

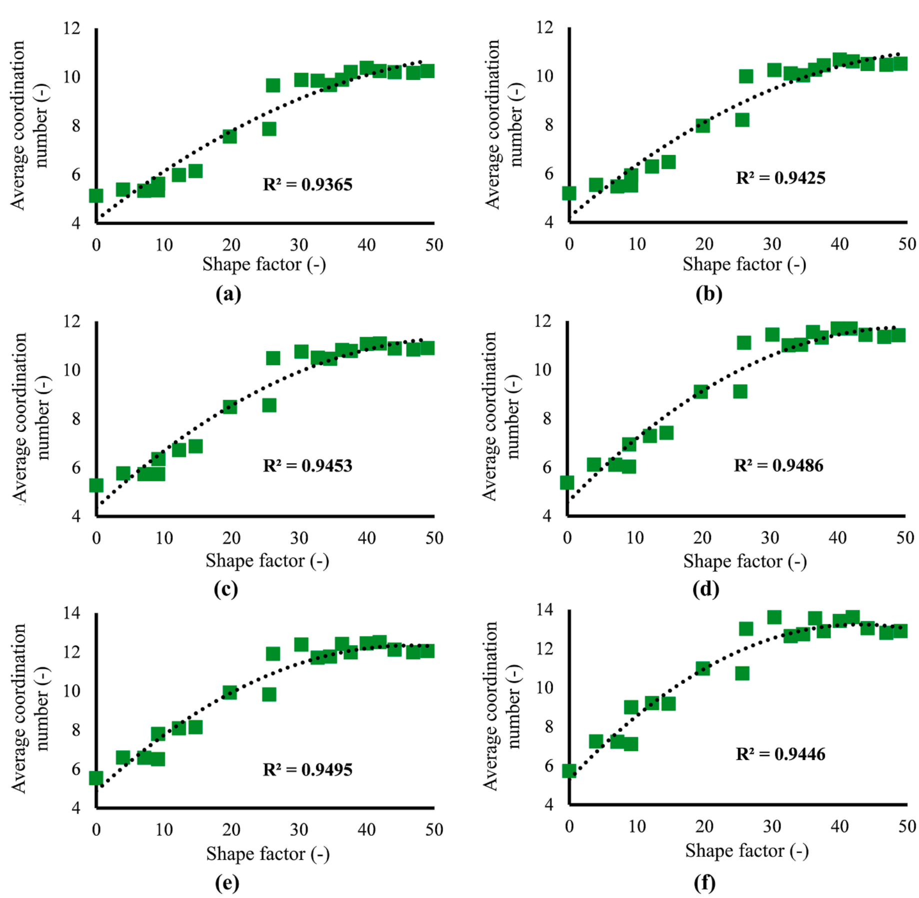


**Fig. 13.** The $\overline{Z}$–SF relationship for predefined vertical stresses, (a) 0.1 MPa, (b) 0.2 MPa, (c) 0.4 MPa, (d) 0.8 MPa, (e) 1.6 MPa, (f) 3.2 MPa.

curves is preserved; as SF increases, the regular increase in $\overline{Z}$ continues steadily. This regularity suggests that the coordination number exhibits shape-dependent variation even at low stress levels.

Although a slight increase in absolute $\overline{Z}$ values was observed at 1.6 and 3.2 MPa, the overall shape of the curves did not change significantly. This indicates a relatively weak stress dependence of the average coordination number within the investigated range. In other words, while stress is associated with modest increases in $\overline{Z}$, the sensitivity of the coordination number to particle shape is maintained across stress levels. The fact that the $R^2$ values are very similar across the six stress levels also supports this observation.

These findings are consistent with the low stress-sensitivity coefficient ($\alpha_Z$) calculated for the coordination number in the next section. Since $\overline{Z}$ is a fundamental microstructural parameter representing the geometry of the contact network, higher SF values are associated with higher coordination numbers; this trend is observed even at low stress levels. The particle-level coordination-number distributions presented in Section 3.4 further indicate that this increase is not limited to a change in the mean value alone, but reflects a broader shift of the particle population toward higher coordination states. Therefore, the relationship between $\overline{Z}$ and SF becomes apparent much earlier and with comparatively weaker sensitivity to stress than the macro-scale modulus–shape relationship.

When these results are considered together, it can be observed that the micro-scale contact arrangement is consistently influenced by particle shape, but its sensitivity to stress is comparatively limited. This provides a basis for scaling the coordination number by only a small exponential factor in the stress-normalization process. Furthermore, the use of normalized parameters ($Z_n$) enables a clearer analysis of the shape-related trend already visible in the microscale response.

### 3.7. Determination of stress-sensitivity exponents and stress-normalization of macro–micro responses

The macro- and micro-scale results obtained at constant stress levels show that increasing vertical stress produces qualitatively different effects on the two parameters. At the macro scale, the fact that M–SF curves diverge significantly only at stresses above 0.4 MPa indicates a strong dependence of stiffness on stress level, while shape-related trends remain limited at low stresses. In contrast, the similar shape of $\overline{Z}$–SF curves at all stress levels at the microscale indicates that the coordination structure's sensitivity to shape is less dependent on stress, and that coordination number retains a comparatively consistent shape-related trend across stress levels. This distinction is also consistent with the contact-scale observations presented in Section 3.4, where the low-stress weak-contact response was less regular, whereas contact-force and coordination-related indicators became more systematic once the contact network was sufficiently developed. This distinct difference in sensitivity between the two scales motivates reducing the stress effect in the quantitative expression of macro- and micro-responses.

For this purpose, log–log regression models were used to determine how the values of the modulus and coordination number scale with stress, and exponential coefficients (α) representing the effect of stress on both parameters were obtained. The analyses revealed $\alpha_M = 0.50$ at the macro scale; this value suggests that the modulus scales approximately with the square root of stress, which is consistent with the stress threshold behavior determined in Section 3.5. At the micro scale, the value $\alpha_Z = 0.085$ was obtained, and the sensitivity of the coordination number to stress was found to be limited, consistent with the slope and trend similarity observed in Section 3.6. Thus, the sensitivity difference between the two-scale mechanical responses was quantified, and the dominant macro-scale stress effect was distinguished from the weak micro-scale stress effect.

Determining these exponential coefficients enabled the construction of normalized descriptors in which the dominant stress-scaling component was reduced for M and $\overline{Z}$. Accordingly, the values of constrained modulus and coordination number were normalized using Equations (18) and (19), respectively.

$$M_n = \frac{M}{\sigma^{0.5}} \tag{18}$$

$$Z_n = \frac{\overline{Z}}{\sigma^{0.085}} \tag{19}$$

The $M_n$ and $Z_n$ values obtained as a result of normalization serve as stress-normalized response descriptors that allow shape-related trends to be compared more directly across different stress levels. In this normalized representation, the strong macro-scale stress threshold effect identified in Section 3.5 is reduced, whereas the more persistent shape-related trend observed in the coordination-number response remains comparatively visible. The contact-scale statistics introduced in Section 3.4 provide complementary evidence for this interpretation by showing that particle shape also modifies force partitioning, mean contact-force scaling, and local overlap distributions. However, the primary stress-normalized macro–micro descriptors in the present framework remain $M_n$ and $Z_n$.

This transformation provides the basis for defining common stress-normalized descriptors prior to regression modeling. The $M_n - SF$ and $Z_n - SF$ regression equations presented in the next section are therefore intended to provide empirical comparative relationships for examining morphology-related compressibility trends within the analyzed particle family, rather than universal predictive expressions.

It should be noted that the present normalization procedure and the resulting stress-sensitivity exponents were derived from a controlled DEM dataset generated under a single modeling configuration. Accordingly, the normalized descriptors should be interpreted as comparative representations within the adopted framework. A full sensitivity analysis with respect to particle count, repeated initial packings, and alternative model settings was beyond the scope of the present study; therefore, the normalized relationships are not presented as fully uncertainty-quantified predictions. Similarly, the additional contact-scale statistics should be interpreted as supporting micro-mechanical evidence for the representative particle models, rather than as independent constitutive descriptors.

### 3.8. Stress-normalized regression models for macro- and micro-scale responses

The evaluation of normalized responses allowed shape-related trends in compressibility to be examined quantitatively, after reducing the dominant influence of vertical stress conditions. $M_n$ for the macro scale and $Z_n$ for the micro scale were correlated solely with SF, and second-degree polynomial regression models were obtained for both variables. This approach provides an empirical framework that summarizes the trends observed in the preceding analyses and allows the role of particle morphology to be examined within a common normalized representation. The contact-scale statistics presented in Section 3.4 provide additional micro-mechanical context for interpreting these normalized macro- and micro-scale relationships; however, the regression models in this section are based on the primary response descriptors $M_n$ and $Z_n$.

At the macro scale, the relationship between normalized tangent modulus values and SF is distinctly non-linear, exhibiting an initially increasing trend followed by a decreasing trend. This trend reflects a non-monotonic dependence of the normalized macro-scale response on particle shape. The obtained regression model captures this trend:

$$M_n = 97.398 + 2.406 \times SF - 0.0368 \times SF^2 \tag{20}$$

The coefficient of determination for this model is $R^2$, which equals 0.866, indicating that SF alone captures a large portion of the variance in the normalized macro-level response in the analyzed dataset. The distribution and regression curves shown in Fig. 14a illustrate the model's agreement with the analyzed trend.

At the micro-scale, the relationship between the normalized coordination number and SF showed a more regular, consistent increase. This suggests a systematic and shape-dependent organization of contacts. The regression model obtained is in the following form and shows close agreement with the trend of the data analyzed in this study:

$$Z_n = 4.78 + 0.291 \times SF - 0.0028 \times SF^2 \quad (21)$$

The coefficient of determination for this model is $R^2 = 0.936$, indicating that the effect of particle morphology on the normalized micro-scale coordination response is better represented in the analyzed dataset than the macro-scale response. The distribution presented in Fig. 14 (b) shows that the role of SF at the micro-scale is more stable across the range investigated.

When both models are evaluated together, it is observed that particle shape consistently influences compressibility behavior at both macro and micro scales. However, this influence results in maximum stiffness at an intermediate SF value at the macro scale, whereas it exhibits a more gradual increase at the micro scale. This difference highlights the distinct nature of the macro- and micro-scale responses. In light of the contact-scale results in Section 3.4, this difference can be interpreted as the outcome of a combined mechanism: increasing SF promotes a denser contact structure, but the associated redistribution of contact force and local overlap does not translate into a continuously increasing macro-scale stiffness. Thus, normalized models provide empirical and comparable descriptions of shape-related trends in the normalized macro- and micro-scale responses within the analyzed particle family.

### 3.9. Statistical reliability and diagnostics of the regression models

The validity of the regression models for normalized macro-scale stiffness ($M_n$) and micro-scale average coordination number ($Z_n$) was evaluated using statistical diagnostics that test the basic assumptions of regression analysis. Accordingly, residual behavior, normality, variance structure, the consistency of the normalized descriptors, and model explanatory power were analyzed separately. These diagnostics were applied to the primary stress-normalized macro- and micro-scale regression models. The additional $k_F$–SF relationship introduced in Section 3.4 was treated as a descriptive contact-scale relationship for the five representative particle models and was therefore evaluated separately in terms of its coefficient of determination and physical consistency with the contact-force trends, rather than through the full diagnostic procedure applied to the primary regression models.

In the $M_n$–SF regression model obtained for the macro-scale response, the mean of the residuals was very close to zero ($\bar{e} = -0.0048$). The standard deviation of the residuals is 2.36, indicating that the model's prediction errors are random and do not contain systematic bias. The distribution of the residuals was examined using the Shapiro–Wilk normality test, yielding $W = 0.9905$ and $p = 0.6126$. This result indicates that the residuals are statistically normally distributed and that the regression function adequately represents the data structure. Furthermore, the exponential coefficient $\alpha_M = 0.50$, determined to reduce the stress effect at the macro scale via logarithmic transformation, is consistent with the stress-scaling behavior identified in Section 3.7. The model's coefficient of determination ($R^2$) equals 0.866, indicating that approximately 87% of the variance in normalized stiffness behavior is explained by SF alone.

In the micro-scale model, the regression equation describing the relationship between the normalized coordination number and SF demonstrated higher accuracy. The average of the residuals ($\bar{e} = 0.0192$) is quite close to zero, and the standard deviation value is 0.613. This indicates that data dispersion is low at the microscale and that the model captures shape-related trends in contact organization. The Shapiro–Wilk test yielded values of $W = 0.9873$ and $p = 0.4477$ for this model. This result indicates that the residuals satisfy the assumption of normal distribution. The $\alpha_Z$ value (0.085) obtained by reducing the stress effect at the micro scale on a logarithmic basis indicates that the coordination number is weakly influenced by stress and that the normalized model retains a comparatively consistent shape-related trend across the investigated stress range. The micro-scale model has a coefficient of determination ($R^2$), which equals 0.936, indicating that 94% of the variability in the coordination number can be explained by particle shape.

In both primary models, the absence of multicollinearity among the independent variables, which can cause problems in multiple linear regression, is supported by VIF values that remain well below the critical thresholds. The residuals are symmetric around zero and show no consistent deviation across stress levels, indicating that the polynomial functions provide an adequate representation of the observed data. These results indicate that the normalized macro- and micro-scale regression equations satisfy the statistical assumptions and provide statistically adequate empirical descriptions of shape-related trends in the normalized response variables within the analyzed dataset. The contact-scale relationships introduced in Section 3.4, including the $k_F$–SF trend, should be interpreted as supplementary descriptive relationships supporting the micro-mechanical interpretation rather than as independently validated predictive regression models. The contact-scale relationships introduced in Section 3.4, including the $k_F$–SF trend, should be interpreted as supplementary descriptive relationships supporting the micro-mechanical interpretation rather than as independently validated predictive regression models. Overall, the diagnostic results support the regression models' statistical reliability and provide a consistent basis for discussing stress-normalized shape-related trends in the following section.

## 4. Discussions

### 4.1. Micro-mechanical interpretation of the stress-normalized shape effects

This study presents a consistent set of observations on how particle

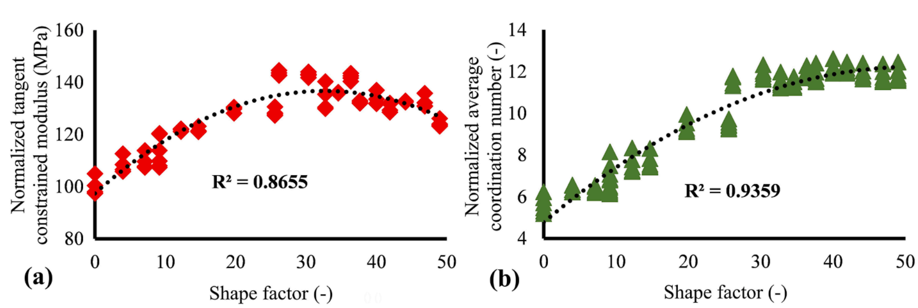


**Fig. 14.** Variation of stress-normalized macro- and micro-scale response indicators with shape factor (SF) in the analyzed dataset: (a) normalized tangent constrained modulus, and (b) normalized average coordination number.

morphology influences mechanical response at both macro and micro scales, using DEM-based analysis of shape-dependent compressibility in granular assemblies. Evaluations based on normalized tangent modulus and normalized average coordination number reveal that particle shape is closely associated with compressibility trends after the dominant stress-scaling component is reduced through normalization. Nonlinear trends at the macro scale, in contrast to more regular, stable increases at the micro scale, highlight the SF effect on various aspects of the mechanical response. These findings suggest that shape parameters in granular materials are not merely geometric features but also fundamental determinants of the organization of contact networks, the continuity of force chains, and micro-rearrangement processes that develop under the load. The additional contact-scale statistics introduced in this study further clarify this interpretation by showing that particle shape also affects weak-contact partitioning, mean normal contact force mobilized per unit vertical stress, coordination-number distributions, and local normal-overlap characteristics.

The relationship between normalized modulus and SF is well described by the regression model ($R^2 = 0.866$), although it shows wider dispersion than the micro-scale relationship. The fundamental reason for this situation is that macro-scale stiffness is sensitive not only to the number of contacts but also to their orientation, the continuity of force chains, local density changes, and rearrangements under stress. Although the increase in SF initially increases stiffness by increasing the average contact number per particle, excessive geometric irregularity above a certain threshold may disrupt the directional integrity of contacts, leading to breaks in force paths. This interpretation is supported by the $k_F$–SF relationship, which shows that the mean normal contact force mobilized per unit vertical stress decreases markedly from the spherical reference toward intermediate SF values, but then tends to approach a plateau-like response with a slight upward tendency at higher SF values. This trend suggests that increasing shape irregularity initially promotes load redistribution over a denser set of contacts, whereas further increases in SF provide a progressively weaker benefit in terms of force redistribution. This interaction between contact enhancement and directional disruption is consistent with the non-monotonic macro-scale response. Furthermore, calculating the tangent modulus as the derivative of the stress–strain curve amplifies small fluctuations in the data and inevitably increases dispersion. Another important point is that at low stress levels (0.1–0.2 MPa), the shape effect has no significant influence on the mechanical response. This region corresponds to a predominantly rearrangement-dominated regime; that is, the particles are essentially rearranging under load, and the contact configurations have not yet stabilized. In contrast, at stresses above 0.4 MPa, the contact networks stabilize, and the shape effect becomes apparent. This transition is also reflected in the weak-contact percentage results: the WCP–SF relationship is relatively scattered at 0.1 MPa, whereas it becomes more systematic at 0.4 MPa and above. Therefore, the stress threshold observed in the macro-scale response is consistent with the development of a more stable force-partitioning structure at the contact scale.

The normalized coordination number ($Z_n$) at the micro scale reflects the effect of particle shape on mechanical behavior more directly. The large $R^2$ value indicates that the coordination number increases consistently with SF and that this relationship shows minimal dispersion. The main reason for this is that the coordination number directly measures contact quantity as a micromechanical indicator. Therefore, shape changes produce a more predictable effect on $\overline{Z}$. However, the newly added coordination-number distribution shows that this trend is not limited to a change in the average value alone. As SF increases, the particle-level coordination-number distribution shifts toward higher coordination states and broadens, indicating that particle shape modifies the distribution of contact states across the assembly. The stress effect is also quite weak on $\overline{Z}$ ($\alpha = 0.085$), resulting in low variability in the normalized micro-scale data. Furthermore, since $\overline{Z}$ is not a derivative quantity like M, fluctuations in the stress–shape response are not amplified. For these reasons, the micro-scale model exhibits higher accuracy and greater stability than the macro-scale model. This finding indicates that macro-scale stiffness is sensitive not only to the number of contacts but also to their directional organization, whereas micro-scale coordination response is more directly associated with geometry. At the same time, the difference between the macro- and micro-scale trends indicates that a higher coordination number alone is not sufficient to ensure a continuously increasing macro-scale stiffness. The overlap statistics support this interpretation by showing that local contact deformation also follows a nonlinear shape-dependent trend: mean and upper-tail normalized overlap values decrease from the spherical reference toward irregular particle shapes, but become less sensitive and slightly increase near the upper end of the investigated SF range. Therefore, the non-monotonic macro-scale stiffness response should be interpreted as the result of a balance between contact-network densification, force partitioning, and local contact deformation, rather than as a direct consequence of coordination number alone.

### 4.2. Micro–macro association of contact-scale indicators

To further support the proposed micro–macro interpretation, the contact-scale indicators obtained from the representative particle models were compared with the corresponding macro-scale stiffness descriptors. Fig. 15 presents two supporting comparisons: the relationship between $k_F$ and the normalized tangent constrained modulus ($M_n$), and the relationship between mean normalized normal overlap $\left(\delta_n^*\right)$ and the tangent constrained modulus ($M$) at 0.8 MPa. These comparisons were not intended to establish independent predictive regression models, but rather to examine whether the contact-scale trends are consistent with the macro-scale stiffness response.

Although non-spherical particles generally exhibit lower $k_F$ values than the spherical reference, the representative-model comparison shows that variations in $k_F$ within the non-spherical subset are positively associated with $M_n$. The $k_F$–$M_n$ relationship therefore indicates that higher normalized stiffness is associated with higher mean normal contact force mobilized per unit vertical stress. This suggests that macro-scale stiffness depends not only on the number of contacts, but also on the degree of force mobilization and the effectiveness of force transmission at the contact scale. In contrast, the $\delta_n^*$–$M$ relationship at 0.8 MPa shows that lower mean normalized normal overlap is generally associated with higher tangent constrained modulus. This indicates that stiffer macro-scale responses tend to accompany more limited local elastic contact deformation.

Taken together, these associations support the interpretation that the non-monotonic macro-scale stiffness response cannot be explained solely by contact-number increase. Instead, it reflects the combined influence of contact-network density, contact-force mobilization, and local contact deformation. Since these comparisons are based on the five representative particle models selected for detailed contact-scale analysis, they should be interpreted as supporting micro–macro associations rather than general predictive relationships.

### 4.3. Implications for shape-dependent compressibility

The literature presents conflicting findings regarding the effect of particle shape on compressibility and stiffness. Some studies suggest that shape irregularity increases stiffness by enhancing interlocking, whereas others indicate that increasing irregularity may also promote local void formation, rearrangement, or less efficient force transfer, thereby leading to a more compressible response. The results of the present study suggest that these apparently contradictory mechanisms need not be mutually exclusive; rather, they may operate simultaneously, with their relative influence depending on stress level and the specific response quantity being considered. In this regard, the combined evaluation of

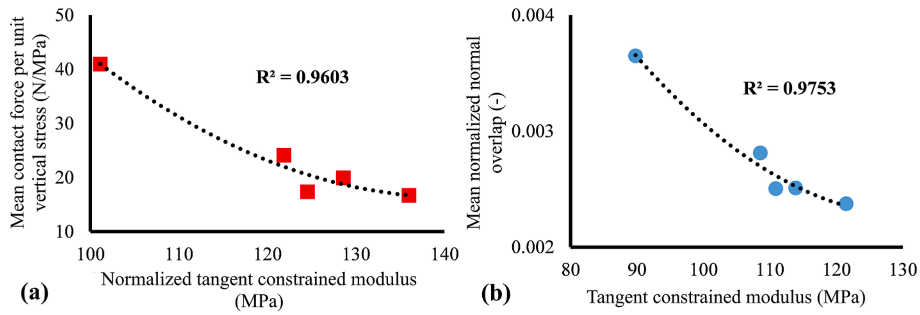


**Fig. 15.** Supporting micro–macro associations for the representative particle models: (a) relationship between the mean normal contact-force coefficient per unit vertical stress ($k_F$) and normalized tangent constrained modulus ($M_n$), and (b) relationship between mean normalized normal overlap $\left(\delta_n^*\right)$ and tangent constrained modulus ($M$) at 0.8 MPa.

the macro-scale modulus, the coordination-number response, and the quantitative contact-scale statistics provides a more nuanced interpretation of the role of particle morphology.

At the micro scale, an increase in SF is consistently associated with a denser contact organization and a broader distribution of force transmission, while the overlap patterns suggest that local deformation is shared among more contacts. The coordination-number distribution confirms that increasing SF shifts the particle population toward higher coordination states, whereas the $k_F$ response indicates that the mean normal force mobilized per unit vertical stress is generally reduced for non-spherical particles compared with the spherical reference. Similarly, the weak-contact percentage and overlap statistics show that shape irregularity modifies both force partitioning and local contact deformation. However, this increase in contact density and redistribution of force/deformation does not translate into a monotonic increase in macro-scale stiffness. Instead, the normalized modulus response indicates that stiffness reaches its maximum at an intermediate SF range and then declines.

This observation suggests that although increasing geometric irregularity enhances contact formation, excessive irregularity may reduce the directional efficiency and continuity of load-bearing contact paths. In other words, the beneficial effect of additional contacts may be partly offset when force transmission becomes less directionally efficient or when local deformation is redistributed in a way that does not further increase macro-scale stiffness. Accordingly, the present results suggest that the compressibility behavior of granular assemblies may reflect a balance between contact enhancement and contact-network efficiency, which may help explain the divergent trends reported in the literature. This interpretation also explains why different indicators respond differently to particle shape: coordination-based metrics emphasize contact formation, whereas modulus-based metrics reflect the combined effect of contact formation, force-chain continuity, force partitioning, and contact-scale deformation.

### *4.4. Interpretive value and limitations of shape descriptor*

In this study, particle shape is represented by the SF parameter calculated from a two-dimensional projection. Although DEM models are constructed symmetrically, the actual three-dimensional morphology of granular materials involves additional geometric components such as corner sharpness, surface roughness, spatial anisotropy, and local curvature. Therefore, the use of three-dimensional shape indicators (e.g., sphericity, convexity, surface roughness) in the future may allow for a more comprehensive assessment of the effect of particle shape on mechanical behavior. In particular, descriptors explicitly accounting for local curvature and true angular corner geometry would be useful for extending the present interpretation to natural granular particles. At the same time, the present projection-based definition of SF provided a practical and internally consistent basis for comparing the idealized particle family considered in this study.

It should also be noted that the adopted clumped-sphere particles do not reproduce true sharp corners or continuously varying natural surface curvature. Therefore, curvature effects were not treated as an independent variable in the present study. Instead, their influence was indirectly reflected through the controlled variation in the SF descriptor and through the resulting contact-force, coordination-number, and normal-overlap statistics. This limitation does not invalidate the comparative trends obtained within the idealized particle family, but it should be considered when extending the findings to natural granular materials.

Initially, the study aimed to use two morphological parameters (SF and AF) together. However, AF's very high correlation with SF ($r = 0.92$) led to multicollinearity issues in the regression models, making it statistically inappropriate to include AF in the model. The results suggest that SF can independently represent shape-induced effects at both macro- and micro scales, indicating that SF is a practical and effective morphological indicator within the adopted descriptor framework. This does not imply that AF is mechanically unimportant; rather, within the present dataset, its explanatory content overlapped strongly with that of SF. Accordingly, the present results should be interpreted as SF-based trends within a controlled and internally consistent morphology framework, rather than as a complete representation of all possible angularity, roughness, and curvature effects in natural granular assemblies.

### *4.5. Scope, limitations, and future directions*

The findings of the present study should be interpreted in light of several methodological limitations. First, the analyzed particle family was intentionally constructed as an idealized, centrally symmetric clumped geometry to enable a controlled comparison of shape effects under consistent DEM conditions. Accordingly, the investigated geometries do not reproduce the full three-dimensional morphological complexity of natural granular particles or the full range of sharp edges, surface roughness, contact forms, and curvature variations that may occur in real granular assemblies. Second, the adopted shape descriptors (SF and AF) were derived from two-dimensional particle projections using a prescribed angular discretization; therefore, the resulting values are specific to the adopted projection and sampling framework.

Third, the DEM configuration was benchmarked against a spherical reference case, whereas the non-spherical particle geometries examined in the parametric analyses were not directly validated against experimental data. Therefore, the non-spherical simulations should be interpreted as a controlled comparative extension of the benchmarked spherical reference model, rather than as directly validated predictions for real non-spherical grains. In addition, the contact model remained within an elastic framework and did not account for particle breakage, crushing, plastic contact deformation, or other irreversible contact-scale damage mechanisms that may become important at higher stress levels.

Accordingly, the highest stress level considered in this study should be viewed as an upper-bound comparative condition within the adopted elastic-contact DEM framework, rather than as a fully realistic representation of particle crushing or damage evolution. Furthermore, although a consistent DEM setup was used for all particle shapes, the influence of specimen size, wall effects, repeated initial packings, and other model settings was not quantified through a full sensitivity or uncertainty analysis. Therefore, the reported regression relationships should be interpreted as comparative empirical trends within the analyzed particle family rather than as fully uncertainty-quantified predictive laws.

The contact-scale analyses should also be interpreted within their intended scope. The visual contact-force and normal-overlap maps were restricted to representative particle shapes, extracted from a central slice of the specimen, and evaluated at a single intermediate stress level for clarity. However, the quantitative contact-scale statistics introduced in the revised analysis were calculated from all active contacts in the full specimen for the selected representative particle models. These statistics were added to strengthen the micro-scale interpretation, but they were not intended to replace full validation against experimental measurements or to establish independent constitutive laws. Within these limitations, the present study provides a controlled comparative DEM framework for examining shape-dependent compressibility trends and the associated contact-scale force–deformation characteristics. Future studies may expand this framework by using larger assemblies, repeated realizations, alternative particle representations, direct experimental validation for non-spherical geometries, contact models incorporating plasticity, damage, or particle breakage, and more flexible data-driven approaches to examine more complex morphology–mechanics relationships.

## 5. Conclusion

This study investigates the effect of particle shape on the compressibility behavior of granular materials using a DEM-based comparative approach. Accordingly, the study shows that shape-related trends in the macro- and micro-scale responses can be examined more directly within the adopted framework after reducing the dominant stress-scaling component. DEM analyses of particle models with different SF values enabled the role of particle shape in the mechanical response to be evaluated through stress-normalized descriptors. The results obtained show that particle shape is consistently associated with statistically significant variations in both the macro-scale tangent modulus and the micro-scale coordination number within the analyzed particle family. In addition, the revised contact-scale analyses provide quantitative evidence that particle shape also affects weak-contact partitioning, mean normal contact force mobilized per unit vertical stress, coordination-number distributions, and local normal-overlap characteristics.

Normalized tangent modulus values ($M_n$) exhibit a nonlinear relationship with SF, indicating the existence of an intermediate SF value at the macro scale. This situation may be interpreted as reflecting the possibility that particle irregularity increases stiffness by enhancing interlocking on the one hand, but may reduce it by weakening the continuity of contact orientation and force chains beyond a certain threshold. In contrast, the normalized average coordination number ($Z_n$) increased with SF, although this positive effect progressively diminished at higher SF levels. The coordination-number distribution further showed that increasing SF shifts the particle population toward higher coordination states, confirming that the micro-scale response is not limited to a change in the average coordination number alone. The $k_F$–SF relationship indicated that non-spherical particles generally mobilize lower mean normal contact force per unit vertical stress than the spherical reference, while the response becomes less sensitive and tends toward a plateau-like behavior at higher SF levels. The weak-contact percentage and normalized overlap statistics further showed that shape irregularity modifies force partitioning and local contact deformation. The polynomial-based regression equations developed for both models quantitatively describe how SF is associated with compressibility-related response trends and suggest that these trends differ between the macro- and micro-scale descriptors. Taken together, these findings indicate that the non-monotonic macro-scale stiffness response cannot be explained solely by the number of contacts; rather, it reflects the combined effects of contact-network densification, force redistribution, and local contact deformation.

Although the SF used in the study is a morphological indicator based on a two-dimensional projection, it provided a practical representation of shape-related effects at both the macro and micro scales. The high collinearity with AF suggests that excluding AF from the model was statistically appropriate within the present regression framework and that SF retained most of the explanatory information contained in the adopted descriptor pair. This result indicates that SF can be used as a practical shape parameter for comparative analysis within the analyzed particle family. However, considering that three-dimensional shape features in real materials contain more geometric detail, future inclusion of 3D morphological indicators, including descriptors of local curvature, angular corners, and surface roughness, would provide a more comprehensive micromechanical representation.

In conclusion, this study has presented a controlled comparative DEM framework for examining shape-dependent compressibility trends through stress-normalized macro- and micro-scale response descriptors, empirical regression models, and quantitative contact-scale statistics. The obtained models provide an initial empirical basis for comparing morphology-related compressibility trends within the analyzed particle family. The findings should, however, be interpreted in light of the adopted assumptions, including the use of idealized clumped particle geometries, projection-based shape descriptors, spherical-case benchmarking, elastic contact modeling without particle breakage, plastic contact deformation, or crushing, and a single DEM modeling configuration without a full sensitivity or uncertainty analysis. Future research may further benefit from larger assemblies, repeated realizations, alternative particle representations, direct validation for non-spherical geometries, contact models incorporating plasticity or breakage, and more flexible data-driven approaches for examining more complex morphology–mechanics relationships.

## CRediT authorship contribution statement

**Betül Poyraz:** Writing – original draft, Validation, Software, Methodology, Investigation, Formal analysis, Data curation. **Ahmet Talha Gezgin:** Writing – review & editing, Visualization, Supervision, Resources, Methodology, Formal analysis, Conceptualization.

## Declaration of competing interest

The authors declare that they have no known competing financial interests or personal relationships that could have appeared to influence the work reported in this paper.

## References

Alshibli, K. A., & Cil, M. B. (2018). Influence of particle morphology on the friction and dilatancy of sand. *Journal of Geotechnical and Geoenvironmental Engineering, 144*(3). https://doi.org/10.1061/(asce)gt.1943-5606.0001841

Altair Engineering Inc. (2022). *Altair EDEM 2022: Discrete element method software for bulk and granular material simulation*. Altair Engineering Inc.

Altuhafi, F. N., Coop, M. R., & Georgiannou, V. N. (2016). Effect of particle shape on the mechanical behavior of natural sands. *Journal of Geotechnical and Geoenvironmental Engineering, 142*(12). https://doi.org/10.1061/(asce)gt.1943-5606.0001569

Antony, S. J., & Kuhn, M. R. (2004). Influence of particle shape on granular contact signatures and shear strength: New insights from simulations. *International Journal of Solids and Structures, 41*(21), 5863–5870. https://doi.org/10.1016/j.ijsolstr.2004.05.067

Banala, A., Ma, H., & Kumar, A. (2019). Influence of particulate geometry on permeability of porous materials. *Powder Technology, 345*, 704–716. https://doi.org/10.1016/j.powtec.2019.01.064

Basak, R., Manuel Carlevaro, C., Kozlowski, R., Cheng, C., Pugnaloni, L. A., Kramár, M., Zheng, H., Socolar, J. E. S., & Kondic, L. (2021). Two approaches to quantification of force networks in particulate systems. *Journal of Engineering Mechanics, 147*(11). https://doi.org/10.1061/(ASCE)EM.1943-7889.0002003

Burns, S. J., & Hanley, K. J. (2017). Establishing stable time-steps for DEM simulations of non-collinear planar collisions with linear contact laws. *International Journal for Numerical Methods in Engineering, 110*(2), 186–200. https://doi.org/10.1002/nme.5361

Burns, S. J., Piiroinen, P. T., & Hanley, K. J. (2019). Critical time step for DEM simulations of dynamic systems using a Hertzian contact model. *International Journal for Numerical Methods in Engineering, 119*(5), 432–451. https://doi.org/10.1002/nme.6056

Cheng, H., Luding, S., Saitoh, K., & Magnanimo, V. (2020). Elastic wave propagation in dry granular media: Effects of probing characteristics and stress history. *International Journal of Solids and Structures, 187*, 85–99. https://doi.org/10.1016/j.ijsolstr.2019.03.030

Chung, Y.-C. (2006). *Discrete element modelling and experimental validation of a granular solidsubject to different loading conditions [PhD]*. University of Edinburgh.

Cohen, J. (1992). A power primer. *Psychological Bulletin, 112*(1), 155–159. https://doi.org/10.1037/0033-2909.112.1.155

Cundall, P. A., & Strack, O. D. L. (1979). A discrete numerical model for granular assemblies. *Géotechnique, 29*(1), 47–65. https://doi.org/10.1680/geot.1979.29.1.47

Danesh, A., Mirghasemi, A. A., & Palassi, M. (2020). Evaluation of particle shape on direct shear mechanical behavior of ballast assembly using discrete element method (DEM). *Transportation Geotechnics, 23*. https://doi.org/10.1016/j.trgeo.2020.100357

Dimaio, F., & Direnzo, A. (2005). Modelling particle contacts in distinct element SimulationsLinear and non-linear approach. *Chemical Engineering Research and Design, 83*(11), 1287–1297. https://doi.org/10.1205/cherd.05089

Durán, O., Kruyt, N. P., & Luding, S. (2010). Micro-mechanical analysis of deformation characteristics of three-dimensional granular materials. *International Journal of Solids and Structures, 47*(17), 2234–2245. https://doi.org/10.1016/j.ijsolstr.2010.04.014

El-Kassem, B., Salloum, N., Brinz, T., Heider, Y., & Markert, B. (2021). A multivariate regression parametric study on DEM input parameters of free-flowing and cohesive powders with experimental data-based validation. *Computational Particle Mechanics, 8*(1), 87–111. https://doi.org/10.1007/s40571-020-00315-8

Gezgin, A. T. (2025). Multi-scale DEM investigation of the effects of particle shape and size characteristics on the direct shear response of granular materials. *Journal of Innovations in Civil Engineering and Technology, 7*(2), 251–266. https://doi.org/10.60093/jiciviltech.1814761

Gezgin, A. T., Soltanbeigi, B., Altunbas, A., & Cinicioglu, O. (2021). Multi-scale investigation of active failure for various modes of wall movement. *Frontiers of Structural and Civil Engineering, 15*(4), 961–979. https://doi.org/10.1007/s11709-021-0738-4

Gezgin, A. T., Soltanbeigi, B., & Cinicioglu, O. (2022). Discrete-element modelling of pile penetration to reveal influence of soil characteristics. *Proceedings of the Institution of Civil Engineers: Geotechnical Engineering, 175*(4), 365–382. https://doi.org/10.1680/jgeen.20.00134

Hanley, K. J., Huang, X., O'Sullivan, C., & Kwok, F. C. Y. (2014). Temporal variation of contact networks in granular materials. *Granular Matter, 16*(1), 41–54. https://doi.org/10.1007/s10035-013-0470-4

Hatefi, M. H., Arabani, M., Payan, M., Zanganeh Ranjbar, P., Keawsawasvong, S., & Jamsawang, P. (2024). The role of particle shape in the mechanical behavior of granular soils: A state-of-the-art review. In *Results in engineering* (Vol. 24). Elsevier B. V. https://doi.org/10.1016/j.rineng.2024.103572

He, Y., & Guo, F. (2018). Micromechanical analysis on the compaction of tetrahedral particles. *Chemical Engineering Research and Design, 136*, 610–619. https://doi.org/10.1016/j.cherd.2018.06.019

Hill, J. M., & Selvadurai, A. P. S. (2005). *Mathematics and mechanics of granular materials*. Netherlands: Springer. https://doi.org/10.1007/1-4020-4183-7

Ioannidi, P. I., McLafferty, S., Reber, J. E., Morra, G., & Weatherley, D. (2024). Deformation and frictional failure of granular media in 3D analog and numerical experiments. *Pure and Applied Geophysics, 181*(7), 2083–2105. https://doi.org/10.1007/s00024-024-03464-6

Jaeger, H. M., Nagel, S. R., & Behringer, R. P. (1996). Granular solids, liquids, and gases. *Reviews of Modern Physics, 68*(4), 1259–1273. https://doi.org/10.1103/RevModPhys.68.1259

Jiang, M., Yin, Z.-Y., & Shen, Z. (2016). Shear band formation in lunar regolith by discrete element analyses. *Granular Matter, 18*(2), 32. https://doi.org/10.1007/s10035-016-0635-z

Jing, L., & Stephansson, O. (2007). Discrete element methods for granular materials. *Developments in Geotechnical Engineering, 85*, 399–444. https://doi.org/10.1016/S0165-1250(07)85011-5

Karimpour-Fard, M., Rezvani, R., & Selakjani, S. G. (2021). Crushability and compressibility of carbonate and siliceous sands in the one-dimensional oedometer test. *Arabian Journal of Geosciences, 14*(23), 2536. https://doi.org/10.1007/s12517-021-08751-3

Kodicherla, S. P. K., Gong, G., Yang, Z. X., Krabbenhoft, K., Fan, L., Moy, C. K. S., & Wilkinson, S. (2019). The influence of particle elongations on direct shear behaviour of granular materials using DEM. *Granular Matter, 21*(4), 86. https://doi.org/10.1007/s10035-019-0947-x

Koutous, A., & Hilali, E. (2019). Grain shape effects on the mechanical behavior of compacted earth. *Case Studies in Construction Materials, 11*, Article e00303. https://doi.org/10.1016/j.cscm.2019.e00303

La Ragione, L., & Jenkins, J. T. (2009). The influence of particle fluctuations on the average rotation in an idealized granular material. *Journal of the Mechanics and Physics of Solids, 57*(9), 1449–1458. https://doi.org/10.1016/j.jmps.2009.06.005

Lee, C. L., Bililign, E., Azéma, E., & Daniels, K. E. (2025). Loading-dependent microscale measures control bulk properties in granular material: An experimental test of the stress-force-fabric relation. *Physical Review E, 112*(3), Article 035401. https://doi.org/10.1103/rv25-lqdc

Li, X., & Yu, H. S. (2013). On the stress-force-fabric relationship for granular materials. *International Journal of Solids and Structures, 50*(9), 1285–1302. https://doi.org/10.1016/j.ijsolstr.2012.12.023

Liu, B., Cen, W., Yan, G., Scheuermann, A., Zheng, C., & Zhang, P. (2025). Particle shape effects on breakage behaviors in granular materials: A multiscale geotechnical perspective. *Computers and Geotechnics, 187*, Article 107504. https://doi.org/10.1016/j.compgeo.2025.107504

Mata, J. (2011). Interpretation of concrete dam behaviour with artificial neural network and multiple linear regression models. *Engineering Structures, 33*(3), 903–910. https://doi.org/10.1016/j.engstruct.2010.12.011

Mesri, G., & Vardhanabhuti, B. (2009). Compression of granular materials. *Canadian Geotechnical Journal, 46*(4), 369–392. https://doi.org/10.1139/T08-123

Ng, T. T., Zhou, W., Ma, G., & Chang, X. L. (2018). Macroscopic and microscopic behaviors of binary mixtures of different particle shapes and particle sizes. *International Journal of Solids and Structures, 135*, 74–84. https://doi.org/10.1016/j.ijsolstr.2017.11.011

Nie, Z., Fang, C., Gong, J., & Yin, Z. Y. (2020). Exploring the effect of particle shape caused by erosion on the shear behaviour of granular materials via the DEM. *International Journal of Solids and Structures, 202*, 1–11. https://doi.org/10.1016/j.ijsolstr.2020.05.004

O'Sullivan, C. (2011). *Particulate discrete element modelling*. CRC Press. https://doi.org/10.1201/9781482266498

Pearson, K. (1896). VII. Mathematical contributions to the theory of evolution.—Iii. Regression, heredity, and panmixia. *Philosophical Transactions of the Royal Society of London - Series A: Containing Papers of a Mathematical or Physical Character, 187*, 253–318. https://doi.org/10.1098/rsta.1896.0007

Peng, Z., Chen, C., & Wu, L. (2021). Numerical investigation of particle shape effect on sand shear strength. *Arabian Journal for Science and Engineering, 46*(11), 10585–10595. https://doi.org/10.1007/s13369-021-05430-z

Radjai, F., Delenne, J.-Y., Azéma, E., & Roux, S. (2012). Fabric evolution and accessible geometrical states in granular materials. *Granular Matter, 14*(2), 259–264. https://doi.org/10.1007/s10035-012-0321-8

Rojek, J. (2018). Contact modeling in the discrete element method. In A. Popp, & P. Wriggers (Eds.), *Contact modeling for solids and particles* (Vol. 585, pp. 177–228). Springer. https://doi.org/10.1007/978-3-319-90155-8_4.

Santamarina, J. C. (2003). Soil behavior at the microscale: Particle forces. *Soil Behavior and Soft Ground Construction*, 25–56. https://doi.org/10.1061/40659(2003)2

Sarkar, D., Goudarzy, M., & König, D. (2019). An interpretation of the influence of particle shape on the mechanical behavior of granular material. *Granular Matter, 21* (3), 53. https://doi.org/10.1007/s10035-019-0909-3

Shapiro, S. S., & Wilk, M. B. (1965). An analysis of variance test for normality (complete samples). *Biometrika, 52*(3–4), 591–611. https://doi.org/10.1093/biomet/52.3-4.591

Sharma, A., Leib-Day, A. R., Thakur, M. M., & Penumadu, D. (2021). Effect of particle morphology on stiffness, strength and volumetric behavior of rounded and angular natural sand. *Materials, 14*(11), 3023. https://doi.org/10.3390/ma14113023

Sharma, L. K., & Singh, T. N. (2018). Regression-based models for the prediction of unconfined compressive strength of artificially structured soil. *Engineering with Computers, 34*(1), 175–186. https://doi.org/10.1007/s00366-017-0528-8

Sukumaran, B., & Ashmawy, A. K. (2001). Quantitative characterisation of the geometry of discret particles. *Géotechnique, 51*(7), 619–627. https://doi.org/10.1680/geot.2001.51.7.619

Thakur, S. C., Ooi, J. Y., & Ahmadian, H. (2016). Scaling of discrete element model parameters for cohesionless and cohesive solid. *Powder Technology, 293*, 130–137. https://doi.org/10.1016/j.powtec.2015.05.051

Ulusoy, U. (2023). A review of particle shape effects on material properties for various engineering applications: From macro to nanoscale. *Minerals, 13*(1), 91. https://doi.org/10.3390/min13010091

Walsh, S. D. C., & Tordesillas, A. (2006). Injecting particle Scale physics into continuum models of granular materials for large-scale applications. *Earth in Space*, 1–8. https://doi.org/10.1061/40830(188)31, 2006.

Wensrich, C. M. (2014). Stress, stress-asymmetry and contact moments in granular matter. *Granular Matter, 16*(4), 597–608. https://doi.org/10.1007/s10035-014-0484-6

Wiącek, J., Molenda, M., Horabik, J., & Ooi, J. Y. (2012). Influence of grain shape and intergranular friction on material behavior in uniaxial compression: Experimental and DEM modeling. *Powder Technology, 217*, 435–442. https://doi.org/10.1016/j.powtec.2011.10.060

Xu, R., Liu, E., & Li, J. (2024). Multiscale analysis of mechanical properties and kinetic processes in dry granular flow. *Advances in Civil Engineering, 2024*(1). https://doi.org/10.1155/adce/4348417

Zeng, Y., Shi, X., Zhao, J., Bian, X., & Liu, J. (2025). Estimation of compression behavior of granular soils considering initial density effect based on equivalent concept. *Acta Geotechnica, 20*(3), 1035–1048. https://doi.org/10.1007/s11440-024-02429-2

Zhao, L., Deng, M., Zhang, S., Huang, D., Qiao, N., & Gong, J. (2023). Effects of particle shape on triaxial compression behaviours of realistic ballast particles based on M-A-V-L particle shape evaluation system. *Granular Matter, 25*(1), 4. https://doi.org/10.1007/s10035-022-01288-6

Zhao, C., & Li, C. (2025). Characterization of orientational order for arbitrary-shaped particles and its applications in granular assemblies. *International Journal of Solids and Structures, 311*. https://doi.org/10.1016/j.ijsolstr.2025.113257

Zhao, J., Zhao, S., & Luding, S. (2023). The role of particle shape in computational modelling of granular matter. *Nature Reviews Physics, 5*(9), 505–525. https://doi.org/10.1038/s42254-023-00617-9